Automatica 161 (2024) 111452

Contents lists available at ScienceDirect

Automatica

journal homepage: www.elsevier.com/locate/automatica

Local navigation-like functions for safe robot navigation in bounded domains with unknown convex obstacles☆

Hamed Farivarnejad [a,*], Amir Salimi Lafmejani [b], Spring Berman [a]

[a] School for Engineering of Matter, Transport and Energy, Arizona State University, Tempe, AZ, 85287, USA
[b] School of Electrical, Computer and Energy Engineering, Arizona State University, Tempe, AZ, 85287, USA

ARTICLE INFO

Article history:
Received 17 July 2021
Received in revised form 30 July 2023
Accepted 25 October 2023
Available online 22 December 2023

Keywords:
Robot navigation
Obstacle avoidance
Virtual potential field
Switching control

ABSTRACT

In this paper, we propose a controller that stabilizes a holonomic robot with single-integrator dynamics to a target position in a bounded domain, while preventing collisions with convex obstacles. We assume that the robot can measure its own position and heading in a global coordinate frame, as well as its relative position vector to the closest point on each obstacle in its sensing range. The robot has no information about the locations and shapes of the obstacles. We define regions around the boundaries of the obstacles and the domain within which the robot can sense these boundaries, and we associate each region with a virtual potential field that we call a *local navigation-like function (NLF)*, which is only a function of the robot's position and its distance from the corresponding boundary. We also define an NLF for the remaining free space of the domain, and we identify the critical points of the NLFs. Then, we propose a switching control law that drives the robot along the negative gradient of the NLF for the obstacle that is currently closest, or the NLF for the remaining free space if no obstacle is detected. We derive a conservative upper bound on the tunable parameter of the NLFs that guarantees the absence of locally stable equilibrium points, which can trap the robot, if the obstacles' boundaries satisfy a minimum curvature condition. We also analyze the convergence and collision avoidance properties of the switching control law and, using a Lyapunov argument, prove that the robot safely navigates around the obstacles and converges asymptotically to the target position. We validate our analytical results for domains with different obstacle configurations by implementing the controller in both numerical simulations and physical experiments with a nonholonomic mobile robot.

1. Introduction

Numerous algorithmically and mathematically rigorous approaches have been proposed for robot navigation in environments with obstacles, many requiring prior information about the environment. We present a switching control law for safe robot navigation that guarantees obstacle avoidance and convergence to a destination without using any prior information about the obstacles' locations and shapes, instead relying only on the robot's localization and onboard sensor measurements. We first review key developments in control schemes for safe robot navigation, categorized according to the properties of the environment that must be known, and then describe our contribution in the context of this work.

Many existing collision-free navigation control schemes are based on virtual potential fields and require knowledge of the locations and shapes of the obstacles. Early works on such control schemes include Khatib (1986), Kim and Khosla (1992), Koditschek and Rimon (1990), Rimon and Koditschek (1992), Shahidi, Shayman, and Krishnaprasad (1991), with the works Koditschek and Rimon (1990), Rimon and Koditschek (1992) introducing controllers based on potential fields called *navigation functions (NFs)* that produce exact robot navigation to target positions in generalized sphere worlds. Many subsequent works developed NF-based control strategies for diverse scenarios. In Conner, Rizzi, and Choset (2003), a combination of NFs and harmonic potential fields, which satisfy Laplace's equation, is proposed for environments in which the free space can be represented as a chain of connected polygons. Acceleration of the robot's convergence to the target position is achieved in Ogren and Leonard (2005) for dynamic environments by merging an NF-based strategy with the dynamic window approach (Fox, Burgard, & Thrun, 1997), and in Paternain, Mokhtari and Ribeiro (2018) for static environments in which the robot starts near the stable manifold of a saddle point of the NF by using a modified Newton

☆ This research was supported by the Arizona State University Global Security Initiative. The material in this paper was not presented at any conference. This paper was recommended for publication in revised form by Associate Editor C.C. Cheah under the direction of Editor Thomas Parisini.
* Corresponding author.
E-mail addresses: hamed.farivarnejad@asu.edu (H. Farivarnejad), asalimil@asu.edu (A.S. Lafmejani), spring.berman@asu.edu (S. Berman).

https://doi.org/10.1016/j.automatica.2023.111452
0005-1098/

method for nonconvex optimization. The work Filippidis and Kyriakopoulos (2011) presents an algorithm for automatically tuning the parameters of NFs for sphere worlds. In Li and Tanner (2019), NFs are constructed for tracking a dynamic target in environments with star-shaped obstacles. Modified NF-based controllers have been recently designed for robot navigation to the minimum of a globally convex potential function in an environment with convex obstacles (Paternain, Koditschek and Ribeiro, 2018), and to the minimum of a quadratic potential function in environments with ellipsoidal obstacles that may be highly eccentric (flat) (Kumar, Paternain, & Ribeiro, 2019) or star-shaped obstacles (Kumar, Paternain, & Ribeiro, 2020). The works Constantinou and Loizou (2020), Loizou (2017) solve the navigation problem on a known star world using a diffeomorphic transformation from the star world to a point world and its inverse.

Barrier certificates (Prajna, Jadbabaie, & Pappas, 2004) and *barrier functions* (Ames, Xu, Grizzle, & Tabuada, 2017) have been used to develop control schemes that prevent a dynamical system from entering unsafe or undesired regions of its state space, which is the set of obstacles when the control objective is collision-free robot navigation. These approaches require knowledge of the boundaries of the unsafe/undesired regions (i.e., the obstacles). The work Wang, Ames, and Egerstedt (2017) presents a control approach that utilizes barrier certificates to prevent collisions among multiple robots and between robots and static or dynamic obstacles. The centers and radii of circles that bound the obstacles must be known beforehand. Control barrier functions have been used to implement collision avoidance in multi-robot systems (Chen, Singletary, & Ames, 2021) and rigid body networks (Ibuki, Wilson, Ames, & Egerstedt, 2020).

Other collision-free navigation control schemes require only approximate information about the locations and shapes of the obstacles. A sliding mode controller is proposed in Guldner and Utkin (1995) to track the gradient of a potential field that is constructed based on the smallest circle that encloses each obstacle. In Paternain and Ribeiro (2017), the robot follows a stochastic approximation of the gradient of an NF, which requires prior estimates of obstacle locations and shapes according to a probability distribution. Sampling-based control schemes that combine optimization techniques and simultaneous localization and mapping (SLAM) approaches comprise another class of controllers that rely on *a priori* partial and/or approximate information about the environment (Arslan, Pacelli, & Koditschek, 2017; Pierson et al., 2019; Vasilopoulos et al., 2020; Vasilopoulos, Vega-Brown, Arslan, Roy, & Koditschek, 2018).

There are also collision-free navigation control schemes that do not rely on prior information about the shapes and locations of the obstacles, but have limitations on their performance guarantees, use particular types of sensor measurements by the robot, and/or require the robot to continuously update its control inputs via online optimization and continuously update its map of the environment. The potential-based controller designed in Ge and Cui (2000) for cases where the robot's target position is very close to an obstacle, extended in Ge and Cui (2002) to scenarios where the target position and obstacles are moving, does not ensure the absence of all local minima that could trap the robot. The work (Ramírez-Llanos & Martínez, 2019) presents a stochastic source-seeking scheme for a robot that can measure a signal and is allowed to make contact with the boundaries of the environment and obstacles, traveling along these boundaries until it finds a feasible direction to the signal source. In Angélico, Chamon, Paternain, Ribeiro, and Pappas (2021), a sinusoidal extremum seeking control scheme is proposed that guarantees collision-free navigation of a robot in environments with convex obstacles; this approach requires online measurements of the curvature of obstacles that the robot encounters. The work Arslan and Koditschek (2019) presents a sensor-based feedback control law for robot navigation in environments with convex obstacles in which the robot computes a Voronoi diagram for the environment online. Although the obstacles may be unknown, an assumption on their curvature is required (*Assumption 2* in Arslan and Koditschek (2019)).

In this paper, we develop a robot controller that guarantees collision-free navigation to a target location using minimal on-board sensing, without information about obstacle locations and shapes. The proposed controller has a closed-form structure and does not require online projection/optimization and mapping algorithms, which are used in the controllers presented in Vasilopoulos et al. (2020, 2018) and Arslan and Koditschek (2019); thus, it is simpler and less computationally intensive to implement on a robot. Both obstacle avoidance and convergence to the target position are enforced by a term in the controller that is the gradient of a virtual potential field that we refer to as a *local navigation-like function (NLF)*, due to its similarity to navigation functions but its dependence only on local sensor measurements. This control approach is similar to the potential-based control law that we designed in Farivarnejad and Berman (2020) for stabilizing a holonomic robot to a target velocity in an unknown, unbounded environment with strictly convex obstacles. The main contributions of this paper are as follows:

(1) We present a closed-form switching controller for safe navigation of a holonomic mobile robot to a target position in a bounded domain containing convex obstacles that are sufficiently separated and curved. The robot can measure its own position and heading and its relative position vector to the closest point on any obstacles within its sensing range. The robot knows the target position and the size of the domain, but not the locations and shapes of the obstacles, and it has no predefined trajectory.
(2) We prove that the controller drives the robot asymptotically to the target position while preventing collisions with the obstacles and entrapment in local minima.
(3) We validate our theoretical results in numerical simulations and experiments with a mobile robot.

2. Preliminaries and problem statement

We consider a disk-shaped holonomic robot with radius r that moves in a planar bounded domain and has a circular sensing range that extends a distance δ_c from the robot's center. The robot has first-order dynamics (a single-integrator model), $\dot{\boldsymbol{q}} = \boldsymbol{u}$, where $\boldsymbol{q} = (x, y)^T \in \mathbb{R}^2$ denotes the position of the robot's center in a global reference frame and $\boldsymbol{u} \in \mathbb{R}^2$ is the robot's control input. We assume that the domain contains multiple arbitrary convex obstacles. The control objective is for the robot to travel to a target position while avoiding collisions with the obstacles and the domain boundary. We assume that the target position is the origin of the global frame, without loss of generality. We first define several terms.

Definition 1 (*Domain*). A compact, closed and convex subset of $\mathbb{R}^2$, whose interior includes the origin (the target position). The domain and its boundary are denoted by $\mathcal{D}$ and $\partial\mathcal{D}$, respectively. The domain's interior is denoted by $\mathcal{I}(\mathcal{D})$ and is defined as $\mathcal{I}(\mathcal{D}) := \mathcal{D} \setminus \partial\mathcal{D}$.

Definition 2 (*Obstacle*). A compact, closed and convex subset of the domain, which does not intersect the domain's boundary. The domain contains $m \geq 1$ obstacles, which are indexed by $i \in \{1, \ldots, m\}$. Obstacle i and its boundary are denoted by $\mathcal{O}_i$ and $\partial\mathcal{O}_i$, respectively.

Definition 3 (*Free Space*)**.** An open subset of the domain which is obtained by removing the obstacles from the domain's interior, defined as $\mathcal{F} := \mathcal{I}(\mathcal{D}) \setminus \bigcup_{i=1}^{m} \mathcal{O}_i$.

Definition 4 (*Repulsion Space*)**.** Let $\delta_i(\boldsymbol{q})$ be the distance from point $\boldsymbol{q} \in \mathbb{R}^2$ to the boundary of the domain for $i = 0$, or to the boundary of obstacle i for $i \in \{1, \ldots, m\}$. We define the repulsion space $\mathcal{R}_i$ as the following semi-closed subset of the free space $\mathcal{F}$: $\mathcal{R}_i = \{\boldsymbol{q} \in \mathcal{F} \mid 0 < \delta_i(\boldsymbol{q}) \leq \delta_c\}$, $i = 0, 1, \ldots, m$. The repulsion space $\mathcal{R}_0$ is the set of points between $\partial\mathcal{D}$ and the closed curve that is offset from this boundary by a distance δ_c along the inward normal to $\partial\mathcal{D}$. The repulsion space $\mathcal{R}_i$, $i \in \{1, \ldots, m\}$, is the set of points between $\partial\mathcal{O}_i$ and the closed curve that is offset from this boundary by a distance δ_c along the outward normal to $\partial\mathcal{O}_i$. The boundary of $\mathcal{R}_i$ is denoted by $\partial\mathcal{R}_i$.

Definition 5 (*Switching Repulsion Surface*)**.** If $l \geq 2$ repulsion spaces intersect, then the set of points that belong to this intersection and are equidistant from the boundaries of the corresponding obstacles (or the boundary of the domain) is called a switching repulsion surface. If $\mathcal{R}_{\sigma_1}$, ..., $\mathcal{R}_{\sigma_l}$ are intersecting repulsion spaces, where $\{\sigma_1, \ldots, \sigma_l\} \subseteq \{0, 1, \ldots, m\}$, then the corresponding switching repulsion surface is defined as

$$\mathcal{S}_{\sigma_1 \ldots \sigma_l} := \left\{\boldsymbol{q} \in \cap_{i \in \{\sigma_1, \ldots, \sigma_l\}} \mathcal{R}_i \mid \delta_{\sigma_1}(\boldsymbol{q}) = \cdots = \delta_{\sigma_l}(\boldsymbol{q})\right\}.$$

Definition 6 (*Safe Space*)**.** An open subset of the free space which is obtained by removing the repulsion spaces from the free space, defined as $\mathcal{SS} := \mathcal{F} \setminus \bigcup_{i=0}^{m} \mathcal{R}_i$.

Remark 7. The safe space has no intersection with any repulsion space; i.e., $\mathcal{SS} \bigcap \mathcal{R}_i = \varnothing$, $i \in \{0, 1, \ldots, m\}$. Moreover, the safe space and repulsion spaces form a cover of the free space; i.e., $\mathcal{SS} \bigcup \left(\bigcup_{i=0}^{m} \mathcal{R}_i\right) = \mathcal{F}$.

An example domain is shown in Fig. 1, with the associated spaces in Definitions 1–6 illustrated in Fig. 2.

Definition 8 (*Closest Collision Point*)**.** The line from the robot's current position $\boldsymbol{q}$ that is normal to the boundary of obstacle i intersects the boundary at the **closest collision point**. This point is denoted by P_i and its position vector is denoted by $\boldsymbol{q}_{P_i}$, as shown in Fig. 3.

Definition 9 (*Collision Vector*)**.** The vector $\boldsymbol{q} - \boldsymbol{q}_{P_i}$ from the closest collision point to the robot's current position is called the **collision vector**. This vector is denoted by $\boldsymbol{d}_i$, as shown in Fig. 3.

We make the following assumptions about the robot's capabilities. The robot has global localization (e.g., GPS) and has no prior information about the obstacles' locations and shapes. The robot can measure its own heading in the global frame, and it can identify the boundaries of nearby obstacles within its sensing range. We assume that at each time instant, the robot can measure the distance $\delta_i(\boldsymbol{q})$ between its center and the boundary of each obstacle i within its sensing range (e.g., using infrared sensors or LIDAR). This distance is the length of the collision vector $\boldsymbol{d}_i$, according to the *Projection Theorem* (Bertsekas, Nedich, & Ozdaglar, 2003). We also assume that the robot can measure the angle $\phi_{\boldsymbol{d}_i}$ of the vector $-\boldsymbol{d}_i$ in its body-fixed frame, e.g., using LIDAR. By adding $\phi_{\boldsymbol{d}_i} + \pi$ rad to the robot's heading in the global frame, the robot can obtain the angle of $\boldsymbol{d}_i$ in the global frame, which we denote by $\theta_{\boldsymbol{d}_i}$.

We also make the following three assumptions. The first, *Assumption 1* in Arslan and Koditschek (2019), enforces a minimum inter-obstacle spacing such that the robot can navigate between any two obstacles. The second defines the (minimal) prior information that the robot has about the environment. The third specifies that the obstacles' boundaries satisfy a minimum curvature condition.

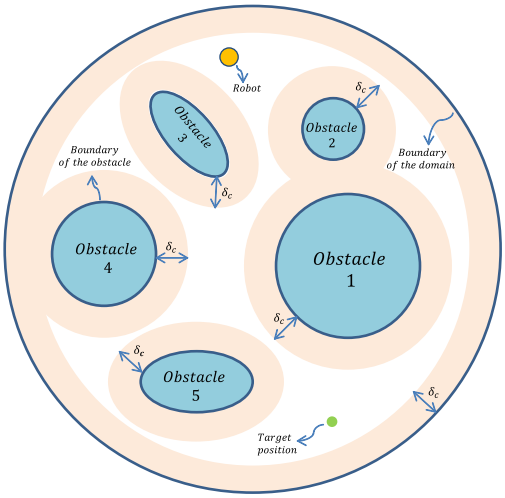

Fig. 1. A circular domain with convex obstacles and the regions that define their associated repulsion spaces.

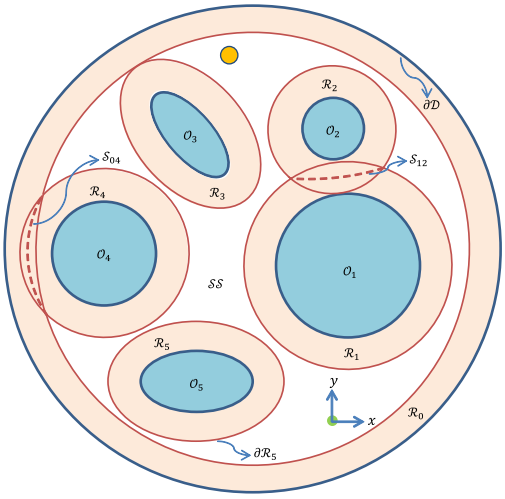

Fig. 2. Different spaces for the environment shown in Fig. 1.

Assumption 10. The shortest distance between the boundaries of each pair of obstacles, and the shortest distance between the boundary of each obstacle and the domain boundary, both exceed the robot's diameter, $2r$.

Assumption 11. The only information provided to the robot is the target position and the size of the domain, defined as the diameter of the smallest circle that contains it. The radius of this circle is denoted by $r_{\mathcal{D}}$.

Assumption 12. For each obstacle, the curvature κ at every point along the obstacle's boundary is strictly greater than $1/r_{\mathcal{D}}$ (see Appendix F.)

Given the robot's local sensor measurements and its minimal information about the environment, we aim to design a control law that can solve the following problem.

Problem 13. We consider a bounded domain, defined as in Definition 1, whose boundary $\partial\mathcal{D}$ is described by $\beta_0(x, y) =$

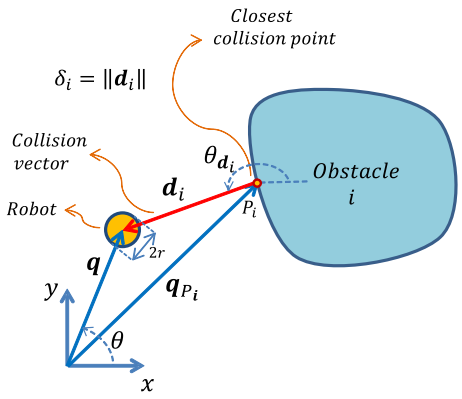

Fig. 3. Illustration of the closest collision point, the collision vector, and their associated variables.

0, where $\beta_0 : \mathbb{R}^2 \mapsto \mathbb{R}$ is a smooth function. The domain contains a finite number $m \geq 1$ of convex obstacles, defined as in Definition 2, with arbitrary boundaries described by $\beta_i(x, y) = 0$, $i \in \{1, \ldots, m\}$, where each function $\beta_i : \mathbb{R}^2 \mapsto \mathbb{R}$ is at least twice continuously differentiable. The robot's target position is in $\mathcal{F}$ and is assumed to be the origin of the global reference frame, without loss of generality. Given Assumptions 10, 11, and 12 and the robot's initial position, which is in the free space $\mathcal{F}$, we design a robot control law that uses only local measurements available to the robot to achieve the following **objectives**: the robot must **(1)** asymptotically converge to the target position; **(2)** not collide with any obstacle or the domain boundary $\partial\mathcal{D}$; and **(3)** never become trapped by any set of obstacles or between obstacles and $\partial\mathcal{D}$.

3. Local Navigation-Like Functions (NLFs)

The construction of a *navigation function (NF)* in the sense of Rimon–Koditschek (Rimon & Koditschek, 1992) over a bounded domain requires prior knowledge of equations that describe the boundaries of the domain and the obstacles that it contains. Moreover, it is necessary to know the number of obstacles in order to tune the parameter κ of the NF (Eq. (10), Rimon and Koditschek (1992)) such that the NF has no local minima that could trap the robot before it reaches its target position. However, in scenarios where robots must navigate an uncertain or completely unknown environment, this information is not available beforehand. To overcome this limitation, we define functions that are similar in form to the NFs in Rimon and Koditschek (1992) but that depend only on locally sensed information. We refer to these functions as *local navigation-like functions (NLFs)*. The NLFs are defined in association with the safe space and each of the repulsion spaces, and they are designed in such a way that: (1) their gradients form a vector field over $\mathcal{F}$ such that a control law that steers the robot in the opposite direction of the vector field at its current position will achieve the objectives described in Problem 13; and (2) to calculate the gradient of an NLF, a robot only needs its on-board measurements of its global position and the collision vectors associated with obstacles within its sensing range. We next define the NLFs and establish properties of their critical points through analysis of their gradients and Hessians. The proofs of all theoretical results in this section are provided in the Appendix.

3.1. Safe space navigation-like function

The safe space NLF, $\varphi_{\mathcal{SS}} : \mathcal{SS} \to [0, 1)$, is defined as

$$\varphi_{\mathcal{SS}}(\boldsymbol{q}) = (\boldsymbol{q}^T\boldsymbol{q})/(\boldsymbol{q}^T\boldsymbol{q} + 1). \tag{1}$$

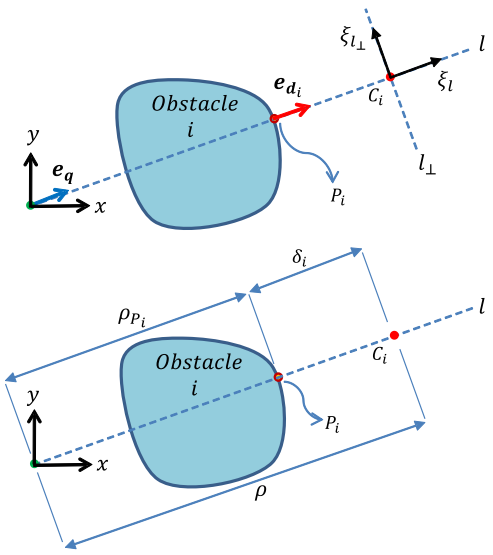

Fig. 4. An illustration of a non-zero norm critical point (C_i) with the associated parameters (ρ, ρ_{P_i}, and δ_i), the closest collision point (P_i), and the local $\xi_l - \xi_{l_\perp}$ coordinate system.

Proposition 14. *If the target position (the origin) is located in the safe space $\mathcal{SS}$, then it is the only critical point of $\varphi_{\mathcal{SS}}$ and, further, is the global minimum of $\varphi_{\mathcal{SS}}$. Otherwise, $\varphi_{\mathcal{SS}}$ has no critical point.*

Remark 15. Given the form of $\nabla\varphi_{\mathcal{SS}}$ in Eq. (A.1), the robot requires only measurements of its own position $\boldsymbol{q}$ to calculate the gradient of $\varphi_{\mathcal{SS}}$.

3.2. Repulsion space navigation-like function

The NLF $\varphi_{\mathcal{R}_i}$ for repulsion space $\mathcal{R}_i$ is defined as

$$\varphi_{\mathcal{R}_i}(\boldsymbol{q}) = (\boldsymbol{q}^T\boldsymbol{q})/(\boldsymbol{q}^T\boldsymbol{q} + g(\delta_i)), \tag{2}$$

where $g(\delta_i) : \mathbb{R}_{>0} \mapsto \mathbb{R}_{>0}$ is the following function of the robot's distance from the boundary of the domain for $i = 0$ or the boundary of obstacle $i \in \{1, \ldots, m\}$:

$$g(\delta_i) = (\delta_i/\delta_c)^k, \tag{3}$$

in which $\delta_i := \|\boldsymbol{d}_i\|$, δ_c is the radius of the robot's sensing range, and k is a strictly positive real number. We can confirm that $\varphi_{\mathcal{R}_i} \in [0, 1)$ for a bounded domain. We note that since δ_i depends on the robot's position $\boldsymbol{q}$, $g(\delta_i)$ is implicitly a function of $\boldsymbol{q}$. The next two propositions characterize the critical points of $\varphi_{\mathcal{R}_i}$.

Proposition 16. *If the target position (the origin) is in $\mathcal{R}_i$, then it is the global minimum of $\varphi_{\mathcal{R}_i}$.*

Proposition 17. *Given the assumption that the target position is $\boldsymbol{q} = \boldsymbol{0}$, $\varphi_{\mathcal{R}_i}$ may have one critical point in $\mathcal{R}_i$ with non-zero norm, i.e. $\boldsymbol{q} \neq \boldsymbol{0}$, if $k \in \mathbb{R}_{>0} - \{2\}$.*

Each obstacle i is associated with one non-zero norm critical point, C_i, which is in $\mathcal{R}_i$ (see Fig. 4). This is because $\varphi_{\mathcal{R}_i}$ is an analytical function in $\mathcal{R}_i \subset \mathbb{R}^2$, which implies that it admits exactly one non-zero norm critical point (Rimon & Koditschek, 1992).

Proposition 18. *The non-zero norm critical point C_i of $\varphi_{\mathcal{R}_i}$ is degenerate for $i = 0, 1, \ldots, m$.*

The following properties are used in the stability analysis of the proposed controller in the next section.

Remark 19. To calculate the gradient of $\varphi_{\mathcal{R}_i}$, the robot only requires measurements of its own position $\boldsymbol{q}$ and the collision vector $\boldsymbol{d}_i$, as indicated by Eqs. (B.1) and (C.1).

Remark 20. The values of the repulsion space NLFs $\varphi_{\mathcal{R}_i}$ for intersecting repulsion spaces $\mathcal{R}_{\sigma_1}, \ldots, \mathcal{R}_{\sigma_l}$ are equal along the switching repulsion surface $\mathcal{S}_{\sigma_1 \ldots \sigma_l}$ (Definition 5), since a robot on this surface is equidistant from the associated obstacles $\mathcal{O}_{\sigma_1}, \ldots, \mathcal{O}_{\sigma_l}$.

4. Controller design and analysis

To define the control law $\boldsymbol{u} \in \mathbb{R}^2$ in the single-integrator model of the robot, $\dot{\boldsymbol{q}} = \boldsymbol{u}$, we first define the set

$$\mathcal{E}_{\boldsymbol{q}} = \underset{\sigma \in \{\mathcal{SS}, \mathcal{R}_0, \mathcal{R}_1, \ldots, \mathcal{R}_m\}}{\arg\max} \{\varphi_\sigma(\boldsymbol{q})\} \tag{4}$$

and denote the cardinality of $\mathcal{E}_{\boldsymbol{q}}$ by $n_{\boldsymbol{q}} := |\mathcal{E}_{\boldsymbol{q}}|$. The proposed control law is given by

$$\boldsymbol{u} = -\frac{1}{n_{\boldsymbol{q}}} \sum_{\eta \in \mathcal{E}_{\boldsymbol{q}}} \nabla \varphi_\eta(\boldsymbol{q}). \tag{5}$$

To execute the control law (5), the robot does not need to measure its distance from every obstacle or identify the particular space it is located in; it only needs to measure and compare its distance from each obstacle within its sensing range. If the robot is in the safe space $\mathcal{SS}$, where all obstacles are outside its sensing range, then the controller uses the gradient of $\varphi_{\mathcal{SS}}$. If the robot is in the union of multiple repulsion spaces $\mathcal{R}_i$ and is not on a switching repulsion surface, then the controller uses the gradient of the NLF $\varphi_{\mathcal{R}_i}$ that has the largest value at the robot's current position. By construction, this NLF is associated with the obstacle i that is closest to the robot (Eq. (2)). Finally, if the robot is on a switching repulsion surface $\mathcal{S}_{\sigma_1 \ldots \sigma_l}$, then the controller uses the average of the gradients of the NLFs $\varphi_{\mathcal{R}_{\sigma_1}}, \ldots, \varphi_{\mathcal{R}_{\sigma_l}}$ of the corresponding intersecting repulsion spaces. The control law (5) is a switching control law, since the gradients of the NLFs could change discontinuously when the robot crosses a switching repulsion surface or moves from a repulsion space to the safe space or vice versa.

Substituting (5) into the robot's equation of motion $\dot{\boldsymbol{q}} = \boldsymbol{u}$, we obtain the closed-loop system, a differential equation with a discontinuous right-hand side:

$$\dot{\boldsymbol{q}} = -\frac{1}{n_{\boldsymbol{q}}} \sum_{\eta \in \mathcal{E}_{\boldsymbol{q}}} \nabla \varphi_\eta(\boldsymbol{q}). \tag{6}$$

Since (5) is a switching control law, the closed-loop system (6) represents a switching system composed of multiple subsystems, each driven by the gradient of the safe space NLF or a repulsion space NLF. The closed-loop robot dynamics in each subsystem are given by

$$\dot{\boldsymbol{q}} = -\nabla \varphi_\sigma(\boldsymbol{q}), \quad \sigma \in \{\mathcal{SS}, \mathcal{R}_0, \mathcal{R}_1, \ldots, \mathcal{R}_m\}. \tag{7}$$

We will analyze the stability, convergence, and collision avoidance properties of system (6) and prove that it achieves the three objectives described in Problem 13. The proofs of some of the theoretical results in this section are provided in the Appendix.

4.1. Stability characteristics of subsystem equilibria

In this subsection, we study the stability of the closed-loop dynamics in an individual subsystem, defined in Eq. (7), by analyzing the stability characteristics of the equilibrium points of the subsystem. The equilibrium points of each subsystem in Eq. (7) are the critical points of the NLF φ_σ corresponding to that subsystem. To investigate the stability properties of these critical points, we apply Lyapunov's indirect method. Linearizing Eq. (7) about the position $\boldsymbol{q}^*$ of a critical point of φ_σ, we obtain:

$$\dot{\boldsymbol{q}} = \left(-\nabla^2 \varphi_\sigma(\boldsymbol{q}^*)\right) \boldsymbol{q}, \quad \sigma \in \{\mathcal{SS}, \mathcal{R}_0, \mathcal{R}_1, \ldots, \mathcal{R}_m\}. \tag{8}$$

Given linearized model (8), we now analyze the eigenvalues of the Hessian of the corresponding NLF φ_σ at $\boldsymbol{q}^*$ and apply the results in Propositions 14, 16, 17, and 18.

Proposition 21. *The origin is an asymptotically stable equilibrium point if it is located in either the safe space or the union of the repulsion spaces.*

Proof. This is concluded from Propositions 14 and 16, where we proved the positive definiteness of the Hessian at the origin. Thus, the negative of the Hessian in Eq. (8) has strictly negative eigenvalues at the origin. □

Non-zero norm critical points of repulsion space NLFs $\varphi_{\mathcal{R}_i}$ are other equilibrium points of the subsystems in Eq. (7). As proved in Proposition 18, these critical points are degenerate, since their corresponding Hessian matrices each have one zero eigenvalue and one positive eigenvalue. This means that the negative of the Hessian in Eq. (8) has one zero eigenvalue and one negative eigenvalue, and therefore linearization about the equilibrium points cannot be used to determine their stability properties. Instead, we use the *center manifold theorem* (Khalil, 1996) to investigate their stability properties. We will use the following two lemmas in this stability analysis.

Lemma 22. *Let $\boldsymbol{q}^*$ be the position of the non-zero norm critical point of the NLF $\varphi_{\mathcal{R}_i}$, $i \in \{0, 1, \ldots, m\}$, in the global reference frame. We define l as the line through the origin and $\boldsymbol{q}^*$ and $l_\perp$ as the line perpendicular to l, as illustrated in Fig. 4. Then $l_\perp$ and l are the center manifold and stable manifold, respectively, of the corresponding subsystem in (7) ($\sigma = \mathcal{R}_i$) in a neighborhood of $\boldsymbol{q}^*$.*

Lemma 23. *We define a subset $\mathcal{B}_{l_\perp}(\boldsymbol{q}^*, \epsilon)$ of the center manifold as $\mathcal{B}_{l_\perp}(\boldsymbol{q}^*, \epsilon) = \{\boldsymbol{q} \in l_\perp \mid \|\boldsymbol{q} - \boldsymbol{q}^*\| < \epsilon, \ \epsilon > 0\}$. If the obstacle's boundary has sufficiently large curvature (Assumption 12) at the closest collision point that corresponds to $\boldsymbol{q}^*$, then there exists a finite $\epsilon > 0$ for which $\varphi_{\mathcal{R}_i}(\boldsymbol{q})$ is maximal at $\boldsymbol{q}^*$ for all $\boldsymbol{q} \in \mathcal{B}_{l_\perp}(\boldsymbol{q}^*, \epsilon)$.*

Proposition 24. *Given Assumption 12, the non-zero norm critical point of $\varphi_{\mathcal{R}_i}$, $i \in \{0, 1, \ldots, m\}$, is an unstable equilibrium of the subsystem in Eq. (7) with $\sigma = \mathcal{R}_i$.*

Proof. The existence of a center manifold and a stable manifold in a neighborhood of a non-zero norm critical point (Lemma 22), and the fact that $\varphi_{\mathcal{R}_i}(\boldsymbol{q})$ is maximal at $\boldsymbol{q}^*$ for all $\boldsymbol{q}$ along the center manifold within a distance ϵ of $\boldsymbol{q}^*$ if Assumption 12 holds (Lemma 23), show that there is no neighborhood of $\boldsymbol{q}^*$ in $\mathbb{R}^2$ for which $\varphi_{\mathcal{R}_i}(\boldsymbol{q}^*)$ is a local minimum. Thus, no basin of attraction can be established for $\boldsymbol{q}^*$, and it is therefore unstable.[1] □

4.2. Absence of equilibria on the switching surfaces

In this subsection, we investigate the existence of locally stable equilibrium points, which could entrap the robot, and derive conditions that guarantee the absence of such equilibrium points from all switching surfaces in the domain. As stated earlier, the robot moves according to Eq. (7) in each subsystem of the

[1] Although $\boldsymbol{q}^*$ is not technically a saddle point, its stability properties resemble those of a saddle point. It is stable for trajectories that start in a set of measure zero (the stable manifold, l) and unstable for trajectories that start outside l.

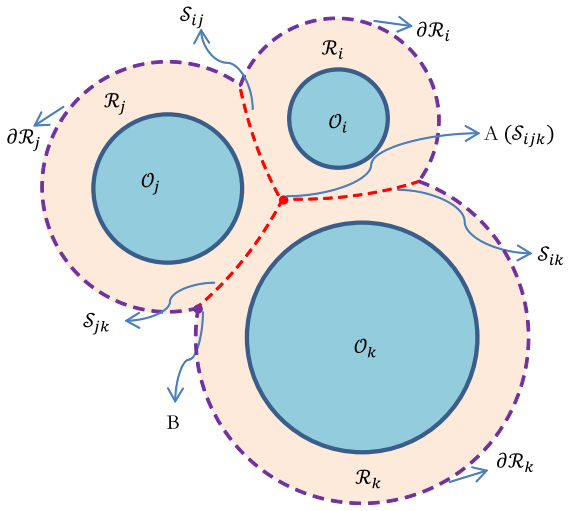

Fig. 5. Illustration of switching repulsion surfaces (*red dashed lines*) and switching surfaces between the safe space and repulsion spaces (*purple dashed lines*). (For interpretation of the references to color in this figure, the reader is referred to the web version of this article.).

switching system (6). The equilibrium points of each subsystem were characterized in Section 4.1. The subsystem indexed by $\sigma \in \{\mathcal{SS}, \mathcal{R}_0, \ldots, \mathcal{R}_m\}$ is active when the robot's position $\boldsymbol{q}$ is in the space σ. A classical (continuously differentiable) solution of Eq. (6), which gives the robot's trajectory $\boldsymbol{q}(t)$, can be obtained as long as the robot evolves in a single subsystem. The active subsystem switches from σ_1 to σ_2 when the robot leaves space σ_1 and enters space σ_2. This *state-dependent* switching creates switching surfaces in the robot's state space. System (6) gives rise to two types of switching surfaces, illustrated in Fig. 5: switching repulsion surfaces (Definition 5), and switching surfaces between the safe space and repulsion spaces. On a switching surface, Eq. (6) can have equilibrium points, depending on the directions of the gradients $\nabla\varphi_\sigma$ associated with the spaces σ that share the switching surface. These equilibrium points may be stable and therefore entrap the robot. In this subsection, we derive conditions that guarantee the absence of equilibrium points on both types of switching surfaces.

4.2.1. Switching repulsion surfaces

If two repulsion spaces $\mathcal{R}_i$ and $\mathcal{R}_j$ intersect, then a switching repulsion surface $\mathcal{S}_{ij}$ exists. This implies that the gradient $-\nabla\varphi_{\mathcal{R}_i}$ drives the dynamics of the robot when it is on the side of the switching surface that contains obstacle i, and $-\nabla\varphi_{\mathcal{R}_j}$ drives its dynamics when it is on the side that contains obstacle j. The closed-loop system (6) can have two types of solutions, depending on the directions of the gradients $-\nabla\varphi_{\mathcal{R}_i}$ and $-\nabla\varphi_{\mathcal{R}_j}$ with respect to the switching surface. If the components of $-\nabla\varphi_{\mathcal{R}_i}$ and $-\nabla\varphi_{\mathcal{R}_j}$ that are normal to the switching surface are pointing in the same direction, then the solution of the closed-loop system is a *Carathéodory* solution. In this case, the system trajectory passes through the switching surface, and no equilibrium point exists on the switching surface. If the two components that are normal to the switching surface point in opposite directions, then the system has a *Filippov* solution that satisfies the following *differential inclusion* (Liberzon, 2003), defined in terms of a convex combination of $-\nabla\varphi_{\mathcal{R}_i}$ and $-\nabla\varphi_{\mathcal{R}_j}$:

$$\dot{\boldsymbol{q}} \in \boldsymbol{\Upsilon}(\boldsymbol{q}) := \{\alpha(-\nabla\varphi_{\mathcal{R}_i}(\boldsymbol{q})) + (1-\alpha)(-\nabla\varphi_{\mathcal{R}_j}(\boldsymbol{q})) : \alpha \in [0,1]\}. \tag{9}$$

Eq. (9) describes the dynamics of the robot as:

$$\dot{\boldsymbol{q}} = \begin{cases} -\nabla\varphi_{\mathcal{R}_i}(\boldsymbol{q}), & \boldsymbol{q} \in \mathcal{R}_i\ , \quad \delta_i < \delta_j \\ \alpha(-\nabla\varphi_{\mathcal{R}_i}(\boldsymbol{q})) + (1-\alpha)(-\nabla\varphi_{\mathcal{R}_j}(\boldsymbol{q})), & \boldsymbol{q} \in \mathcal{S}_{ij} \\ -\nabla\varphi_{\mathcal{R}_j}(\boldsymbol{q}), & \boldsymbol{q} \in \mathcal{R}_j\ , \quad \delta_i > \delta_j \end{cases} \tag{10}$$

Since the components of $-\nabla\varphi_{\mathcal{R}_i}$ and $-\nabla\varphi_{\mathcal{R}_j}$ that are normal to the switching surface point in opposite directions, the system trajectory corresponding to the Filippov solution can only evolve on the switching surface. At the point where the trajectory reaches the switching surface, there is a unique convex combination of $-\nabla\varphi_{\mathcal{R}_i}$ and $-\nabla\varphi_{\mathcal{R}_j}$ (i.e., a unique value for α in Eq. (9)) that is tangent to the surface, which defines the direction of $\boldsymbol{\Upsilon}(\boldsymbol{q})$ on the surface. The Filippov solution at each point on the switching surface is represented by the value of α for which $\boldsymbol{\Upsilon}(\boldsymbol{q})$ is tangent to the surface at that point.

A trajectory corresponding to a Filippov solution often chatters about the switching surface. Unlike a sliding mode controller, our controller is not designed to stabilize the system trajectories to the switching surface; although chattering may occur, the robot will eventually leave the switching surface if the parameter k is bounded by the constant derived in Proposition 25. Under this condition, the closed-loop system has no equilibria on the switching surface, which ensures that the robot will not become trapped between two obstacles.

Proposition 25. *Suppose that a switching repulsion surface $\mathcal{S}_{ij}$ exists. Given Assumptions 10 and 11, no equilibrium point exists on $\mathcal{S}_{ij}$ if k in Eq. (3) is chosen to satisfy $k < r/(r_{\mathcal{D}} - r)$.*

This result can be generalized to a switching repulsion surface that is associated with more than two obstacles (e.g., point A in Fig. 5), as stated in the next corollary.

Corollary 26. *Consider a switching repulsion surface $\mathcal{S}_{\sigma_1\ldots\sigma_l}$, $\{\sigma_1, \ldots, \sigma_l\} \subseteq \{0, 1, \ldots, m\}$, that lies within the intersection of $l \geq 3$ repulsion spaces $\mathcal{R}_{\sigma_1}, \ldots, \mathcal{R}_{\sigma_l}$. The condition in Eq. (G.4) ensures that no equilibrium point exists on this switching surface.*

4.2.2. Switching surfaces between the safe space and repulsion spaces

Suppose that a segment of the boundary $\partial\mathcal{R}_i$ of repulsion space $\mathcal{R}_i$ is adjacent to the safe space $\mathcal{SS}$, forming a switching surface. This implies that the gradient $-\nabla\varphi_{\mathcal{R}_i}$ drives the dynamics of the robot when it is on the side of the switching surface that contains obstacle i, and $-\nabla\varphi_{\mathcal{SS}}$ drives its dynamics when it is on the other side, i.e. in $\mathcal{SS}$. The discussion in Section 4.2.1 about the discontinuity of the right-hand side of Eq. (6) and the two possible types of solutions to this equation (Carathéodory and Filippov) also applies to this type of switching surface. Thus, as in Section 4.2.1, we consider a Filippov solution to the closed-loop system (6) on the switching surface between $\mathcal{R}_i$ and $\mathcal{SS}$ and derive conditions under which the system has no equilibria on this switching surface, given in the next proposition.

Proposition 27. *Given Assumption 11, no equilibrium point exists on the switching surface between repulsion space $\mathcal{R}_i$ and the safe space $\mathcal{SS}$ if k in Eq. (3) is chosen to satisfy $k < \delta_c/(r_{\mathcal{D}} - r)$.*

As we show next, this result can be generalized to a switching surface that is adjacent to $\mathcal{SS}$ and is associated with more than one obstacle (e.g., point B in Fig. 5).

Corollary 28. *Consider a switching surface that lies within the intersection of the boundaries of $l \geq 2$ repulsion spaces $\mathcal{R}_{\sigma_1}, \ldots, \mathcal{R}_{\sigma_l}$, $\{\sigma_1, \ldots, \sigma_l\} \subseteq \{0, 1, \ldots, m\}$, and is adjacent to $\mathcal{SS}$. The condition in Eq. (I.5) ensures that no equilibrium point exists on this switching surface.*

The following theorem guarantees the absence of equilibrium points on all switching surfaces in the domain.

Theorem 29. *Given Assumptions 10 and 11, no equilibrium point exists on any switching surface in the domain if k in Eq. (3) satisfies the following condition:*

$$k < \min(r, \delta_c)/(r_{\mathcal{D}} - r). \tag{11}$$

Proof. The result follows from Corollaries 26 and 28. □

4.3. Convergence analysis

In this subsection, we study the convergence properties of the entire closed-loop system (6), which has a switching structure, and prove the robot's almost global asymptotic stability to the target position. As discussed in Section 4.2, system (6) is a differential equation with a discontinuous right-hand side, which does not satisfy the Lipschitz continuity condition. This implies that we cannot directly apply Lyapunov's stability theorems or LaSalle's invariance principle to analyze the stability and convergence properties of the system. To this end, we apply the concept of *multiple Lyapunov functions*, which has been developed for stability analysis of switching systems (Ch. 3 in Liberzon (2003)). We first state the following two lemmas, which are used in the analysis afterward.

Lemma 30. *Given the closed-loop system (6), which is composed of the subsystems in Eq. (7), the function* $V_\sigma(\boldsymbol{q}) := \varphi_\sigma(\boldsymbol{q})$, $\sigma \in \{\mathcal{SS}, \mathcal{R}_0, \mathcal{R}_1, \ldots, \mathcal{R}_m\}$, *is continuous over every solution* $\boldsymbol{q}(t)$ *of Eq. (6) for* $t \geq 0$.

Lemma 31. *Assume that the robot does not start at a critical point of* $\varphi_\sigma(\boldsymbol{q})$. *Given the subsystems indexed by* $\sigma \in \{\mathcal{SS}, \mathcal{R}_0, \ldots, \mathcal{R}_m\}$ *in Eq. (7), we define* $t_{\sigma,1}$ *and* $t_{\sigma,2}$ *as the times when the robot enters and leaves space* σ, *respectively; i.e.,* $\boldsymbol{q}(t) \in \sigma$ *for all* $t \in [t_{\sigma,1}, t_{\sigma,2})$.[2] *Then for every space* σ, *the function* V_σ *defined in Lemma 30 strictly decreases over the time interval* $[t_{\sigma,1}, t_{\sigma,2})$. *Moreover, the robot's trajectory converges to the origin (the target position) if the origin is in* σ. *Finally, if there is a non-zero norm critical point* $\boldsymbol{q}^*$ *in* σ, *and the robot's trajectory starts on the stable manifold* l *of* $\boldsymbol{q}^*$ *(i.e.,* $\boldsymbol{q}(0) \in l$*), then the robot's trajectory converges to* $\boldsymbol{q}^*$.

We define the set $\mathcal{L}$ as the union of the stable manifolds l of all the non-zero norm critical points in $\mathcal{F}$. We now state the main result of this subsection.

Theorem 32. *Consider the switching closed-loop system (6) with parameter k satisfying Eq. (11). Every trajectory of system (6) that starts in* $\mathcal{F}$ *and outside* $\mathcal{L}$ *asymptotically converges to the origin (the target position), and the origin is almost globally asymptotically stable.*

4.4. Collision avoidance analysis

Here, we prove that under the control law (5), the robot never collides with the obstacles or the domain boundary. Theorem 32 directly implies the following result.

Corollary 33. *Consider the closed-loop system (6) with parameter k satisfying Eq. (11). The free space* $\mathcal{F}$ *is a positively invariant set for any trajectory that starts in* $\mathcal{F}$, *and consequently no collision occurs between the robot and the boundaries of the obstacles and the domain.*

[2] If the robot starts in space σ, rather than entering it from another space, then $t_{\sigma,1} = 0$. If the robot converges to a point in σ, rather than leaving σ, then $t_{\sigma,2} = \infty$.

5. Simulation results

We validated our theoretical results with MATLAB simulations of a holonomic robot with $r = 0.1$ m and $\delta_c = 0.5$ m. The robot must navigate from $\boldsymbol{q}(0) = [-3 \;\; 3]^T$ to $\boldsymbol{q}_T = [0 \;\; 0]^T$ in a domain of radius $r_{\mathcal{D}} = 2.5$ m with six obstacles, whose configuration satisfies Assumption 10. We set $k = 0.04$, which satisfies the bound in Eq. (11). In the first simulation, $\boldsymbol{q}_T$ is in $\mathcal{R}_0$. Fig. 6 plots the robot's trajectory $\boldsymbol{q}(t)$ *(red dashed line)* for $t \in [0, \; 12]$ s, and Fig. 7 plots the corresponding time evolution of $\varphi_\sigma(\boldsymbol{q}(t))$. Fig. 6 shows that the robot avoids the obstacles *(blue circles and ellipses)* and converges to $\boldsymbol{q}_T$ within 10 s. The robot's convergence to $\boldsymbol{q}_T$ coincides with the monotonic convergence of $\varphi_\sigma(\boldsymbol{q}(t))$ to 0 in Fig. 7, and the fact that $\varphi_\sigma(\boldsymbol{q}(t)) < 1$ over the entire trajectory confirms that the robot never collides with the boundaries of the obstacles or the domain, where $\varphi_\sigma(\boldsymbol{q}) = 1$. In the second simulation, $\boldsymbol{q}_T$ is in $\mathcal{SS}$. Figs. 8 and 9 plot $\boldsymbol{q}(t)$ and $\varphi_\sigma(\boldsymbol{q}(t))$, respectively, for $t \in [0, \; 12]$ s. Again, the robot converges to $\boldsymbol{q}_T$ within 10 s without colliding with boundaries; i.e., $\varphi_\sigma(\boldsymbol{q}(t))$ converges monotonically to 0 while remaining below 1. Figs. 7 and 9 show that in both simulations, the robot has a slow rate of convergence to $\boldsymbol{q}_T$ during the first 7 s. This is because the force of attraction to $\boldsymbol{q}_T$ is much smaller than the net repulsion force from the obstacles during this time. The convergence rate can be increased by reducing k, which would create smaller repulsion forces that allow the robot to travel closer to the boundaries.

6. Experimental implementation and results

We also tested our controller on a commercial nonholonomic robot, the TurtleBot3 Burger robot (Robotis, 2021). We first used our method in Lafmejani, Farivarnejad, and Berman (2021) to convert the controller, which is designed for a holonomic robot, into one that can be implemented on a nonholonomic robot. This method can be applied to any feedback controller, such as the control law (5), that is based on the gradient of a potential field φ and is designed for a single-integrator holonomic robot model in $\mathbb{R}^2$ to achieve position stabilization and obstacle avoidance. Given a nonholonomic robot with a reference point P at the midpoint of the axis connecting its wheels, the unicycle kinematic model of the robot is:

$$\dot{x} = v\cos(\psi), \quad \dot{y} = v\sin(\psi), \quad \dot{\psi} = \omega, \tag{12}$$

where $\boldsymbol{x} := [x \;\; y]^T$ is the position of point P in the global reference frame, v is the speed of this point, ψ is the robot's heading angle in the global frame, and ω is the robot's angular velocity. Defining $\mu := \|\nabla\varphi\|$, $\varrho := \|\boldsymbol{x}\|$, and $\gamma := \tan^{-1}(\frac{y}{x})$, the control law (5) is converted into:

$$v = k_v\mu, \quad \omega = k_\omega \frac{\mu}{\varrho}\sin(\psi - \gamma), \tag{13}$$

where k_v and k_ω are controller gains. It is proved in Lafmejani et al. (2021) that if $k_v < 0$ and $k_\omega = 2k_v$, then control law (13) drives the robot to the origin from almost any initial position in the domain while preventing it from colliding with the obstacles and the domain's boundary. This control law has no discontinuities since it uses continuous functions (trigonometric functions of the robot's heading angle) that produce a smooth robot trajectory.

The robot estimates its global pose using a fusion of odometry and IMU sensor data, as described in Lafmejani et al. (2021). It uses its onboard LIDAR to measure its distance to obstacles within its sensing range, which we truncate from the maximum range of 3.5 m to $\delta_c = 0.6$ m. We tested the controller in two scenarios, which differ in the number of obstacles, the robot's initial position $\boldsymbol{q}(0)$, and the value of k. A video of the experiments

is available at Autonomous Collective Systems Lab YouTube channel (2021). *Scenario 1*, in which $\boldsymbol{q}(0) = [-3.75 \quad 2.0]^{\mathrm{T}}$ m and $k = 0.15$, demonstrates that the robot's trajectory can switch between Carathéodory and Filippov solutions of Eq. (6) (see Section 4.2.1). Fig. 10 shows that the robot's trajectory *(dashed line)* chatters when it first passes between obstacles due to its repeated crossing of the switching surface between them, and does not chatter when it next passes between obstacles since they are relatively far apart. After avoiding the obstacles, the robot reaches the goal point at 359 s. *Scenario 2*, in which $\boldsymbol{q}(0) = [-3.75 \quad 2.25]^{\mathrm{T}}$ and $k = 0.12$ or 0.1, illustrates the effect of k on the robot's convergence rate to the goal: when k is decreased, this rate increases (see Section 5). Figs. 11 and 12 show that the robot reaches the goal at 198 s when $k = 0.12$ and at 124 s when $k = 0.1$.

7. Conclusion

We have designed a control scheme for collision-free navigation of a holonomic disk-shaped robot with single-integrator dynamics in a bounded convex domain that contains unknown convex obstacles. We introduced virtual potential fields called *navigation-like functions* and proposed a switching control law based on the negative gradient of these functions. The control law only requires the robots' local sensor measurements and does not rely on any information about the obstacles' locations and shapes. Moreover, it does not require the robot to solve online optimization problems or to continuously update a map of the environment. These features allow the proposed controller to be implemented in a computationally efficient manner. We analyzed the stability and convergence properties of the robot's closed-loop dynamics and derived bounds on the controller parameter that ensure the absence of local minima that could trap the robot.

One direction for future work is to modify the controller for navigation in domains that have a non-convex boundary and/or contain non-convex obstacles, and for which Assumptions 10 and 12 do not hold. This requires deriving conditions that guarantee the absence of local minima that could arise in concave regions of the obstacles and domain boundary and in narrow channels in the free space. Future work can also include modifying the control law in Eq. (5) to eliminate chattering when the robot passes over a switching surface. One potential solution is to use *hysteresis switching*, which enforces the property that two consecutive switching events are separated by a finite time interval, resulting in a hybrid closed-loop system with both continuous and discrete state variables (Liberzon, 2003). Another possible extension is to adapt the controller to achieve collision-free navigation in three dimensions.

Acknowledgment

We thank Ashish Kumar for his help in making obstacles for the experiments.

Appendix A. Proof of Proposition 14

The gradient of $\varphi_{\mathcal{SS}}$ can be calculated as:

$$\nabla\varphi_{\mathcal{SS}} = 2\boldsymbol{q}/(\boldsymbol{q}^T\boldsymbol{q}+1)^2. \tag{A.1}$$

Setting $\nabla\varphi_{\mathcal{SS}} = \boldsymbol{0}$, $\boldsymbol{q} = \boldsymbol{0}$ is the only solution, provided it is in $\mathcal{SS}$. In addition, the Hessian of $\varphi_{\mathcal{SS}}$ is given by:

$$\nabla^2\varphi_{\mathcal{SS}} = 2\left((\boldsymbol{q}^T\boldsymbol{q}+1)\boldsymbol{I} - 4\boldsymbol{q}\boldsymbol{q}^T\right)/(\boldsymbol{q}^T\boldsymbol{q}+1)^3, \tag{A.2}$$

where $\boldsymbol{I} \in \mathbb{R}^{2\times 2}$ is the identity matrix. The Hessian at $\boldsymbol{q} = \boldsymbol{0}$ is equal to $2\boldsymbol{I}$, a positive definite matrix. Also, from Eq. (1), $\varphi_{\mathcal{SS}}$ is zero at $\boldsymbol{q} = \boldsymbol{0}$ and positive everywhere else. Thus, $\boldsymbol{q} = \boldsymbol{0}$ is the global minimum of $\varphi_{\mathcal{SS}}$. If $\boldsymbol{q} = \boldsymbol{0}$ is not in $\mathcal{SS}$, then $\varphi_{\mathcal{SS}}$ has no critical point.

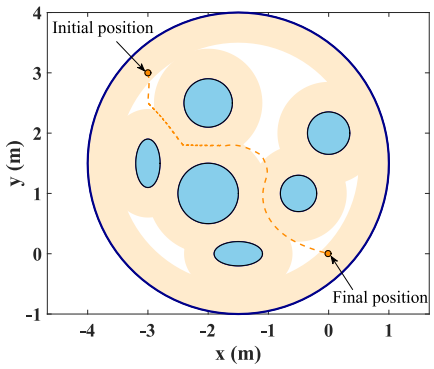

Fig. 6. Robot trajectory in a simulation with $\boldsymbol{q}_T \in \mathcal{R}_0$. (For interpretation of the references to color in this figure, the reader is referred to the web version of this article.).

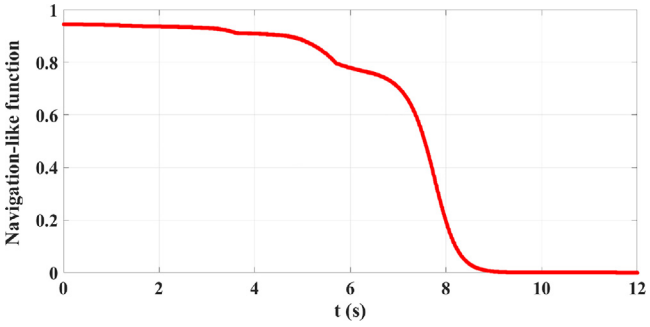

Fig. 7. Value of $\varphi_\sigma(\boldsymbol{q}(t))$ along the trajectory in Fig. 6.

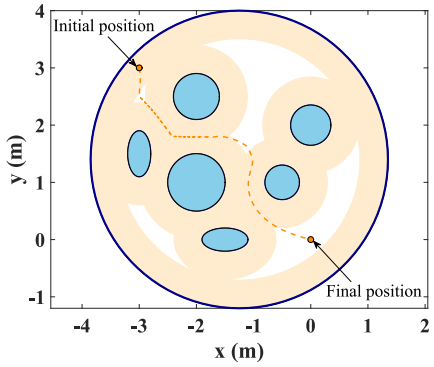

Fig. 8. Robot trajectory in a simulation with $\boldsymbol{q}_T \in \mathcal{SS}$.

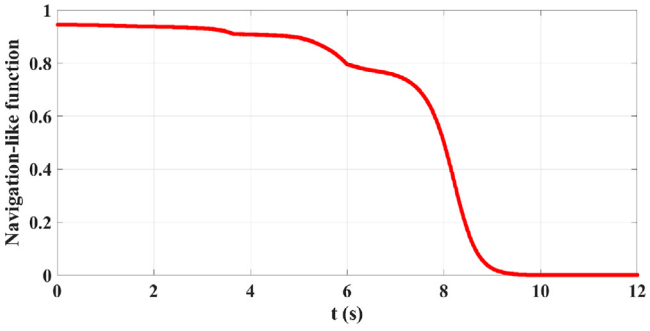

Fig. 9. Value of $\varphi_\sigma(\boldsymbol{q}(t))$ along the trajectory in Fig. 8.

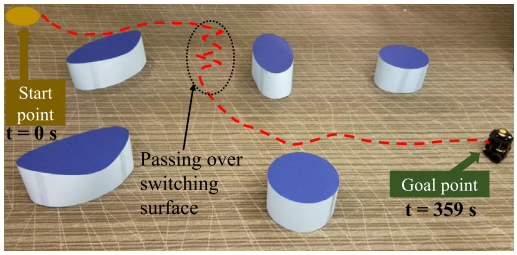

Fig. 10. Robot trajectory for a run of *Scenario 1*; $k = 0.15$.

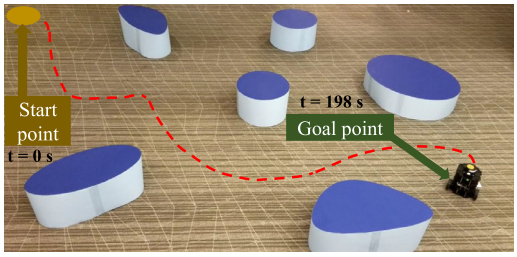

Fig. 11. Robot trajectory for a run of *Scenario 2*; $k = 0.12$.

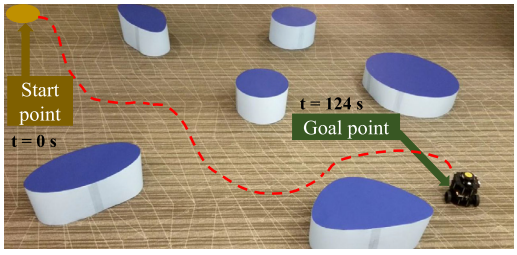

Fig. 12. Robot trajectory for a run of *Scenario 2*; $k = 0.1$.

Appendix B. Proof of Proposition 16

The gradient of $\varphi_{\mathcal{R}_i}$ is calculated as:

$$\nabla\varphi_{\mathcal{R}_i} = \frac{2g(\delta_i)\boldsymbol{q} - (\boldsymbol{q}^T\boldsymbol{q})\nabla g(\delta_i)}{\left(\boldsymbol{q}^T\boldsymbol{q} + g(\delta_i)\right)^2}. \tag{B.1}$$

Setting $\nabla\varphi_{\mathcal{R}_i} = \boldsymbol{0}$ to find the critical points leads to:

$$2g(\delta_i)\boldsymbol{q} - (\boldsymbol{q}^T\boldsymbol{q})\nabla g(\delta_i) = \boldsymbol{0}. \tag{B.2}$$

A solution to Eq. (B.2) is $\boldsymbol{q} = \boldsymbol{0}$. The Hessian of $\varphi_{\mathcal{R}_i}$ is:

$$\nabla^2\varphi_{\mathcal{R}_i} = (\boldsymbol{N}_1(\boldsymbol{q}) - \boldsymbol{N}_2(\boldsymbol{q}))/(\boldsymbol{q}^T\boldsymbol{q} + g)^3, \tag{B.3}$$

in which $\boldsymbol{N}_1(\boldsymbol{q}), \boldsymbol{N}_2(\boldsymbol{q}) \in \mathbb{R}^{2\times 2}$ are:

$$\begin{aligned}\boldsymbol{N}_1(\boldsymbol{q}) &= (\rho^2 + g)\left(2g\boldsymbol{I} - \rho^2\nabla^2 g + 2(\boldsymbol{q}\nabla g^T - \nabla g\boldsymbol{q}^T)\right),\\ \boldsymbol{N}_2(\boldsymbol{q}) &= 2\left(2g\boldsymbol{q}\boldsymbol{q}^T + 2g\boldsymbol{q}\nabla g^T - \rho^2\nabla g\boldsymbol{q}^T - \rho^2\nabla g\nabla g^T\right),\end{aligned} \tag{B.4}$$

where $\rho := \|\boldsymbol{q}\|$. For $\boldsymbol{q} = \boldsymbol{0}$, $\boldsymbol{N}_1 = 2g^2\boldsymbol{I}$ and $\boldsymbol{N}_2 = \boldsymbol{0}$, and so the Hessian at the origin is simplified to $\nabla^2\varphi_{\mathcal{R}_i}\,|_{\boldsymbol{q}=\boldsymbol{0}} = \frac{2}{g}\boldsymbol{I}$, a positive definite matrix. Also, by construction, $\varphi_{\mathcal{R}_i}$ is zero at the origin and positive everywhere else in $\mathcal{R}_i$. Thus, the origin is the global minimum of $\varphi_{\mathcal{R}_i}$.

Appendix C. Proof of Proposition 17

The gradient of $g(\delta_i)$ in Eq. (B.2), which is the derivative of g with respect to $\boldsymbol{q}$, is equal to $\nabla_{\boldsymbol{d}_i} g(\delta_i)$, since $\boldsymbol{q} = \boldsymbol{d}_i + \boldsymbol{q}_{P_i}$ and g is only a function of δ_i, where $\delta_i = \|\boldsymbol{d}_i\|$ (similar to Eq. (7) in Tanner, Jadbabaie, and Pappas (2003), and as proved in Appendix A of Farivarnejad and Berman (2020)). Also, $\nabla_{\boldsymbol{d}_i} g(\delta_i)$ can be calculated as:

$$\nabla_{\boldsymbol{d}_i} g(\delta_i) = g'(\delta_i)\boldsymbol{e}_{\boldsymbol{d}_i}, \tag{C.1}$$

in which $g'(\delta_i)$ is the derivative of g with respect to δ_i, and $\boldsymbol{e}_{\boldsymbol{d}_i}$ is the unit vector along $\boldsymbol{d}_i$. Substituting Eq. (C.1) into Eq. (B.2) and incorporating the expressions for $g(\delta_i)$ and $g'(\delta_i)$, Eq. (B.2) can be rewritten as:

$$\frac{\rho\delta_i^{k-1}}{\delta_c^k}(2\delta_i\boldsymbol{e}_{\boldsymbol{q}} - \rho k\boldsymbol{e}_{\boldsymbol{d}_i}) = \boldsymbol{0}, \tag{C.2}$$

where $\rho := \|\boldsymbol{q}\|$ and $\boldsymbol{e}_{\boldsymbol{q}}$ is the unit vector along $\boldsymbol{q}$. Therefore, the non-zero norm solutions of Eq. (B.2) are the solutions of:

$$2\delta_i\boldsymbol{e}_{\boldsymbol{q}} - \rho k\boldsymbol{e}_{\boldsymbol{d}_i} = \boldsymbol{0}. \tag{C.3}$$

Given that this is a vector equation, $\boldsymbol{e}_{\boldsymbol{q}}$ and $\boldsymbol{e}_{\boldsymbol{d}_i}$ are unit vectors, and $\delta_i, \rho, k > 0$, Eq. (C.3) implies that at the non-zero norm critical points of $\varphi_{\mathcal{R}_i}$,

$$\boldsymbol{e}_{\boldsymbol{q}} = \boldsymbol{e}_{\boldsymbol{d}_i}, \tag{C.4}$$

$$2\delta_i = \rho k. \tag{C.5}$$

The vector $\boldsymbol{e}_{\boldsymbol{d}_i}$ is normal to the boundary of obstacle i and points outward from this boundary (Fig. 3). Thus, the existence of a solution to Eqs. (C.4) and (C.5) depends on the geometry of obstacle i and the obstacle's position and orientation with respect to the target position. If $k = 2$, then from Eq. (C.5) we have that $\rho = \delta_i$, which implies that Eq. (C.3) has a solution only if the origin (the target point) is on the boundary of the obstacle, i.e., coincident with the closest collision point P_i (see Fig. 4). However, this would violate objective (2) in Problem 13, since the robot would collide with the obstacle in its attempt to reach the target point. We note that the dependency of a solution to Eq. (C.3) on ρ implies its dependency on the target position, not the origin of the coordinate system. We have assumed the target position to be the origin, without loss of generality, only to simplify the mathematical derivations.

Appendix D. Proof of Proposition 18

We found that Eqs. (C.4)–(C.5) hold at the non-zero norm critical point of $\varphi_{\mathcal{R}_i}$. Incorporating Eqs. (C.4)–(C.5) into the Hessian of $\varphi_{\mathcal{R}_i}$, defined by Eqs. (B.3)–(B.4), we can confirm that $\boldsymbol{N}_2 = \boldsymbol{0}$ at the critical point, and the Hessian is simplified to

$$\nabla^2\varphi_{\mathcal{R}_i}\,|_{\boldsymbol{q}=\mathcal{C}_i} = \left(2g\boldsymbol{I} - \rho^2\nabla^2 g\right)/(\boldsymbol{q}^T\boldsymbol{q} + g)^2. \tag{D.1}$$

The Hessian of g is obtained from $\nabla^2 g = \frac{\partial}{\partial\boldsymbol{q}}(\nabla g)$. Given Eq. (C.1), the Hessian of g can be rewritten as

$$\nabla^2 g(\delta_i) = \frac{\partial}{\partial\boldsymbol{q}}\left(g'(\delta_i)\boldsymbol{e}_{\boldsymbol{d}_i}\right) = g''(\delta_i)\boldsymbol{e}_{\boldsymbol{d}_i}\boldsymbol{e}_{\boldsymbol{d}_i}^T + g'(\delta_i)\left(\frac{\partial\boldsymbol{e}_{\boldsymbol{d}_i}}{\partial\boldsymbol{q}}\right). \tag{D.2}$$

Denoting the angle of $\boldsymbol{e}_{\boldsymbol{d}_i}$ in the global reference frame by $\theta_{\boldsymbol{d}_i}$ (see Fig. 3), and incorporating the equation for the second derivative of $g(\delta_i)$ with respect to δ_i, the first term on the right-hand side of Eq. (D.2) is calculated as:

$$g''(\delta_i)\boldsymbol{e}_{\boldsymbol{d}_i}\boldsymbol{e}_{\boldsymbol{d}_i}^T = \frac{k(k-1)}{\delta_c^k}\delta_i^{(k-2)}\begin{bmatrix}\cos^2(\theta_{\boldsymbol{d}_i}) & \cos(\theta_{\boldsymbol{d}_i})\sin(\theta_{\boldsymbol{d}_i})\\ \cos(\theta_{\boldsymbol{d}_i})\sin(\theta_{\boldsymbol{d}_i}) & \sin^2(\theta_{\boldsymbol{d}_i})\end{bmatrix}.$$

Furthermore, by the chain rule, the second term on the right-hand side of Eq. (D.2) can be rewritten as:

$$g'(\delta_i)\left(\frac{\partial\boldsymbol{e}_{\boldsymbol{d}_i}}{\partial\boldsymbol{q}}\right) = \frac{k}{\delta_c^k}\delta_i^{(k-1)}\left(\frac{\partial\boldsymbol{e}_{\boldsymbol{d}_i}}{\partial\boldsymbol{e}_{\boldsymbol{q}}}\right)\left(\frac{\partial\boldsymbol{e}_{\boldsymbol{q}}}{\partial\boldsymbol{q}}\right). \tag{D.3}$$

The vectors $\boldsymbol{e}_{\boldsymbol{d}_i}$ and $\boldsymbol{e}_{\boldsymbol{q}}$ are related via the equation $\boldsymbol{e}_{\boldsymbol{d}_i} = \boldsymbol{R}(\alpha_i)\boldsymbol{e}_{\boldsymbol{q}}$, where $\boldsymbol{R}(\alpha_i) \in \mathbb{R}^2$ is a rotation matrix and $\alpha_i := \theta - \theta_{\boldsymbol{d}_i}$, with θ denoting the angle of $\boldsymbol{q}$ with respect to the global frame (see Fig. 3). Hence, in Eq. (D.3), $\partial \boldsymbol{e}_{\boldsymbol{d}_i}/\partial \boldsymbol{e}_{\boldsymbol{q}} = \boldsymbol{R}(\alpha_i)$. In addition, we can calculate that:

$$\frac{\partial \boldsymbol{e}_{\boldsymbol{q}}}{\partial \boldsymbol{q}} = \frac{1}{\rho}\begin{bmatrix} \sin^2(\theta) & -\cos(\theta)\sin(\theta) \\ -\cos(\theta)\sin(\theta) & \cos^2(\theta) \end{bmatrix}. \tag{D.4}$$

At the non-zero norm critical point, $\boldsymbol{e}_{\boldsymbol{q}} = \boldsymbol{e}_{\boldsymbol{d}_i}$ (see Eq. (C.4)), implying that $\theta = \theta_{\boldsymbol{d}_i}$; thus, $\boldsymbol{R}(\alpha_i) = \boldsymbol{R}(0) = \boldsymbol{I}$. Also, ρ in Eq. (D.4) can be replaced by $2\delta_i/k$ from Eq. (C.5). Hence, the Hessian of g can be written as:

$$\nabla^2 g\,|_{\boldsymbol{q}=C_i} = \frac{k\delta_i^{(k-2)}}{\delta_c^k}\begin{bmatrix} (\frac{k}{2}-1)c^2\theta_{\boldsymbol{d}_i} + 1 & (\frac{k}{2}-1)c\theta_{\boldsymbol{d}_i}s\theta_{\boldsymbol{d}_i} \\ (\frac{k}{2}-1)c\theta_{\boldsymbol{d}_i}s\theta_{\boldsymbol{d}_i} & (\frac{k}{2}-1)s^2\theta_{\boldsymbol{d}_i} + 1 \end{bmatrix}, \tag{D.5}$$

where $c\theta_{\boldsymbol{d}_i}$ and $s\theta_{\boldsymbol{d}_i}$ abbreviate $\cos(\theta_{\boldsymbol{d}_i})$ and $\sin(\theta_{\boldsymbol{d}_i})$, respectively. Finally, the Hessian of $\varphi_{\mathcal{R}_i}$ at the non-zero norm critical point can be obtained from Eq. (D.1), and its determinant and trace can be calculated as:

$$\begin{aligned} &\det\left(\nabla^2\varphi_{\mathcal{R}_i}\,|_{\boldsymbol{q}=C_i}\right) = 0 \qquad \forall i \in \{1, 2, \ldots, m\}, \\ &\operatorname{tr}\left(\nabla^2\varphi_{\mathcal{R}_i}\,|_{\boldsymbol{q}=C_i}\right) = \frac{2-k}{2k} \qquad \forall i \in \{1, 2, \ldots, m\}. \end{aligned} \tag{D.6}$$

This demonstrates that at non-zero norm critical points inside $\mathcal{F}$, which exist when $k \in (0, 2)$, one eigenvalue of $\nabla^2\varphi_{\mathcal{R}_i}$ is zero and the other is positive.

Appendix E. Proof of Lemma 22

We define a local coordinate system with its origin located at $\boldsymbol{q}^*$ and its axes denoted by ξ_l and $\xi_{l_\perp}$ (Fig. 4). The axis ξ_l lies along l and points in the direction of $\boldsymbol{e}_{\boldsymbol{d}_i}$, and $\xi_{l_\perp}$ lies along $l_\perp$ and forms a right-handed coordinate system with ξ_l. Given a position $\boldsymbol{q}$ in the global reference frame, we define $\boldsymbol{\xi} := [\xi_l \;\; \xi_{l_\perp}]^T \in \mathbb{R}^2$ as its coordinates in this local reference frame. Denoting the angle of the vector $\boldsymbol{q}^*$ with respect to the global frame by θ^* and the rotation matrix from the local frame to the global frame by $\boldsymbol{R}(\theta^*)$, the transformation of $(\boldsymbol{q} - \boldsymbol{q}^*)$ from the global frame to the local frame is given by

$$\boldsymbol{\xi} = \boldsymbol{R}^T(\theta^*)(\boldsymbol{q} - \boldsymbol{q}^*). \tag{E.1}$$

We define the augmented vectors $\boldsymbol{q}_a := [\boldsymbol{q}^T \;\; 1]^T \in \mathbb{R}^3$, $\boldsymbol{\xi}_a := [\boldsymbol{\xi}^T \;\; 1]^T \in \mathbb{R}^3$. Then Eq. (E.1) can be written as

$$\boldsymbol{\xi}_a = \boldsymbol{T}\boldsymbol{q}_a\,, \quad \boldsymbol{T} = \begin{bmatrix} \boldsymbol{R}^T(\theta^*) & -\boldsymbol{R}^T(\theta^*)\boldsymbol{q}^* \\ \boldsymbol{0}_{1\times 2} & 1 \end{bmatrix} \in \mathbb{R}^{3\times 3}. \tag{E.2}$$

Also, the linearized system in Eq. (8) can be rewritten in an augmented form in terms of $\boldsymbol{q}_a$ as

$$\dot{\boldsymbol{q}}_a = \begin{bmatrix} -\nabla^2\varphi_\sigma(\boldsymbol{q}^*) & \boldsymbol{0}_{2\times 1} \\ \boldsymbol{0}_{1\times 2} & 0 \end{bmatrix}\boldsymbol{q}_a, \tag{E.3}$$

$\sigma \in \{\mathcal{SS}, \mathcal{R}_0, \mathcal{R}_1, \ldots, \mathcal{R}_m\}$. From Eq. (E.2), we have $\boldsymbol{q}_a = \boldsymbol{T}^{-1}\boldsymbol{\xi}_a$, which we use to rewrite Eq. (E.3) in terms of $\boldsymbol{\xi}_a$:

$$\dot{\boldsymbol{\xi}}_a = \boldsymbol{T}\begin{bmatrix} -\nabla^2\varphi_\sigma(\boldsymbol{q}^*) & \boldsymbol{0}_{2\times 1} \\ \boldsymbol{0}_{1\times 2} & 0 \end{bmatrix}\boldsymbol{T}^{-1}\boldsymbol{\xi}_a. \tag{E.4}$$

Multiplying the matrices in Eq. (E.4) and removing the third row and third column (which are all zeros) of the resulting matrix, Eq. (E.4) is simplified to

$$\dot{\boldsymbol{\xi}} = \frac{2-k}{2k}\begin{bmatrix} -1 & 0 \\ 0 & 0 \end{bmatrix}\boldsymbol{\xi}. \tag{E.5}$$

The matrix in the linearized system (E.5) is in block diagonal form and has a negative eigenvalue and a zero eigenvalue for $k \in (0, 2)$. Applying Theorem 8.1 in Khalil (1996), this implies that the corresponding nonlinear system, Eq. (7), has a *center manifold* in the form $\xi_l = h(\xi_{l_\perp})$, where h is a smooth function. Since the vector field of system (7) (the negative gradient of the corresponding NLF, where the gradient is given by Eq. (B.1)) points along l, we can confirm that the only smooth candidate for h is the zero function. Consequently, $\xi_l = 0$, which defines the $\xi_{l_\perp}$-axis of the local coordinate system, is the center manifold of system (7) in a neighborhood of $\boldsymbol{q}^*$. Moreover, the ξ_l-axis, which is associated with the negative eigenvalue of the matrix in Eq. (E.5), is the stable manifold of system (7) in a neighborhood of $\boldsymbol{q}^*$.

Appendix F. Proof of Lemma 23

From Eq. (E.1), $\boldsymbol{q} = \boldsymbol{q}^* + \boldsymbol{R}(\theta^*)\boldsymbol{\xi}$. We insert this expression for $\boldsymbol{q}$ into Eq. (2) and rewrite $\varphi_{\mathcal{R}_i}$ in terms of $\boldsymbol{\xi}$:

$$\varphi_{\mathcal{R}_i}(\boldsymbol{q}) = \frac{\boldsymbol{\xi}^T\boldsymbol{\xi} + 2\boldsymbol{q}^{*T}\boldsymbol{R}^T(\theta^*)\boldsymbol{\xi} + \boldsymbol{q}^{*T}\boldsymbol{q}^*}{\boldsymbol{\xi}^T\boldsymbol{\xi} + 2\boldsymbol{q}^{*T}\boldsymbol{R}^T(\theta^*)\boldsymbol{\xi} + \boldsymbol{q}^{*T}\boldsymbol{q}^* + g(\delta_i)}.$$

The expression $\boldsymbol{q}^{*T}\boldsymbol{R}^T(\theta^*)\boldsymbol{\xi}$ is the inner product of $\boldsymbol{q}^*$ and the representation of $\boldsymbol{\xi}$ in the global frame, $\boldsymbol{q} - \boldsymbol{q}^*$. These two vectors are normal to each other for any $\boldsymbol{q} \in l_\perp$. Hence, at any $\boldsymbol{q} \in \mathcal{B}_{l_\perp}$, $\varphi_{\mathcal{R}_i}(\boldsymbol{q})$ can be simplified to

$$\varphi_{\mathcal{R}_i}|_{\boldsymbol{q}\in\mathcal{B}_{l_\perp}} = (\boldsymbol{\xi}^T\boldsymbol{\xi} + \boldsymbol{q}^{*T}\boldsymbol{q}^*)/(\boldsymbol{\xi}^T\boldsymbol{\xi} + \boldsymbol{q}^{*T}\boldsymbol{q}^* + g(\delta_i)).$$

We know that $\boldsymbol{q}^{*T}\boldsymbol{q}^*$ is constant. Also, we can confirm that δ_i is an implicit function of $\|\boldsymbol{\xi}\|$. Defining $\xi := \|\boldsymbol{\xi}\|$, we can rewrite the equation above as

$$\varphi_{\mathcal{R}_i}|_{\boldsymbol{q}\in\mathcal{B}_{l_\perp}} = (\xi^2 + \rho^{*2})/(\xi^2 + \rho^{*2} + g(\xi)), \tag{F.1}$$

where $\rho^* := \|\boldsymbol{q}^*\|$ and $g(\xi) := g \circ \delta_i(\xi)$. Eq. (F.1) represents the value of $\varphi_{\mathcal{R}_i}(\boldsymbol{q})$ at points $\boldsymbol{q} \in \mathcal{B}_{l_\perp}$ in terms of their distance ξ from the position $\boldsymbol{q}^*$ of the non-zero norm critical point. The derivative of $\varphi_{\mathcal{R}_i}|_{\boldsymbol{q}\in\mathcal{B}_{l_\perp}}$ with respect to ξ is calculated as

$$\frac{d}{d\xi}(\varphi_{\mathcal{R}_i}|_{\boldsymbol{q}\in\mathcal{B}_{l_\perp}}) = \frac{-g'(\xi)\xi^2 + 2g(\xi)\xi - \rho^{*2}g'(\xi)}{\left(\xi^2 + \rho^{*2} + g(\xi)\right)^2}, \tag{F.2}$$

where $g'(\xi) := \frac{d}{d\xi}g(\xi)$ denotes the derivative of $g(\xi)$ with respect to ξ, which, by the chain rule, can be calculated as $\frac{d}{d\xi}g(\xi) = \frac{dg}{d\delta_i}\frac{d\delta_i}{d\xi}$. Let $\delta_i^* := \delta_i(\xi)|_{\xi=0}$ denote the distance between $\boldsymbol{q}^*$ and the closest collision point on the obstacle. It is straightforward to show that:

$$\delta_i^* \;\le\; \delta_i(\xi) \;<\; \Delta_i(\xi) := (\delta_i^{*2} + \xi^2)^{\frac{1}{2}}, \;\; \forall \xi \in [0, \infty). \tag{F.3}$$

We can also confirm that $\frac{d}{d\xi}\Delta_i(\xi)|_{\xi=0} = 0$. Since δ_i^* is constant in Eq. (F.3), the *squeeze theorem* yields $\frac{d}{d\xi}\delta_i(\xi)|_{\xi=0} = 0$. This consequently gives $g'(\xi)|_{\xi=0} = 0$.

We now consider the following two functions:

$$h_1(\xi) := g'(\xi)/g(\xi), \qquad h_2(\xi) := 2\xi/(\xi^2 + \rho^{*2}). \tag{F.4}$$

We can confirm that $h_1(0) = h_2(0) = 0$. Given the continuity of $h_1(\xi)$ and $h_2(\xi)$ and the fact that $\xi \in \mathbb{R}_{\ge 0}$, which is a connected set, we can apply the *comparison lemma* (Khalil, 1996) to show that $h_1(\xi) > h_2(\xi)\ \forall \xi \in (0, \epsilon)$ for some finite $\epsilon > 0$ if

$$h_1'(\xi)|_{\xi=0} \;>\; h_2'(\xi)|_{\xi=0}. \tag{F.5}$$

We calculate that $h_2'(\xi)|_{\xi=0} = \frac{2}{\rho^{*2}}$. Using the fact that $g''(\xi) = \frac{d}{d\xi}(g'(\xi)) = \frac{d}{d\xi}(\frac{dg}{d\delta_i}\frac{d\delta_i}{d\xi})$, we find that

$$h_1'(\xi)|_{\xi=0} \;=\; \frac{1}{g(\xi)|_{\xi=0}}\left.\frac{dg(\delta_i)}{d\delta_i}\right|_{\delta_i=\delta_i^*}\delta_i''(\xi)|_{\xi=0}, \tag{F.6}$$

where $\delta_i''(\xi)$ denotes the second derivative of $\delta_i(\xi)$ with respect to ξ. The Maclaurin series of $\delta_i(\xi)$ is written as:

$$\delta_i(\xi) = \delta_i^* + a_1\xi + a_2\xi^2 + a_3\xi^3 + \cdots, \tag{F.7}$$

where $a_n := \frac{1}{n!}\frac{d^n}{d\xi^n}\delta_i(\xi)|_{\xi=0}$. Given this definition, we have $\delta_i''(\xi)|_{\xi=0} = 2a_2 := \kappa$, the curvature of the obstacle's boundary at the closest collision point. Substituting $\delta_i''(\xi)|_{\xi=0} = \kappa$ into Eq. (F.6), using the resulting expression for $h_1'(\xi)|_{\xi=0}$ in the inequality (F.5), and writing δ_i^* as $\frac{1}{2}k\rho^*$ from Eq. (C.5), we obtain the condition

$$\kappa > 1/\rho^*, \tag{F.8}$$

which guarantees the inequality $h_1(\xi) > h_2(\xi)\ \forall \xi \in (0, \epsilon)$. This inequality can be rewritten as:

$$\frac{-g'(\xi)\xi^2 + 2g(\xi)\xi - \rho^{*^2}g'(\xi)}{g(\xi)\left(\xi^2 + \rho^{*^2}\right)} < 0, \quad \forall \xi \in (0, \epsilon). \tag{F.9}$$

The denominator of the fraction in inequality (F.9) is strictly positive. This implies that the numerator is strictly negative. Moreover, the numerator is the same as the numerator of $\frac{d}{d\xi}(\varphi_{\mathcal{R}_i}|_{\boldsymbol{q}\in\mathcal{B}_{l_\perp}})$ in Eq. (F.2). Given the positiveness of the denominator of $\frac{d}{d\xi}(\varphi_{\mathcal{R}_i}|_{\boldsymbol{q}\in\mathcal{B}_{l_\perp}})$, we can thus conclude that $\frac{d}{d\xi}(\varphi_{\mathcal{R}_i}|_{\boldsymbol{q}\in\mathcal{B}_{l_\perp}})$ is strictly negative, and therefore that $\varphi_{\mathcal{R}_i}|_{\boldsymbol{q}\in\mathcal{B}_{l_\perp}}$ is strictly decreasing for all $\xi \in [0, \epsilon)$. This demonstrates that $\varphi_{\mathcal{R}_i}|_{\boldsymbol{q}\in\mathcal{B}_{l_\perp}}$ is maximal at $\xi = 0$ for all $\xi \in [0, \epsilon)$. Since $\xi = 0$ when $\boldsymbol{q} = \boldsymbol{q}^*$ and $\xi \in [0, \epsilon)$ when $\boldsymbol{q} \in \mathcal{B}_{l_\perp}(\boldsymbol{q}^*, \epsilon)$, we conclude that $\varphi_{\mathcal{R}_i}(\boldsymbol{q})$ is maximal at $\boldsymbol{q}^*$ for all $\boldsymbol{q} \in \mathcal{B}_{l_\perp}(\boldsymbol{q}^*, \epsilon)$. By substituting the maximum possible value for ρ^*, which is $r_{\mathcal{D}}$, into Eq. (F.8), we obtain the following conservative lower bound on κ: $\kappa > 1/r_{\mathcal{D}}$. This inequality imposes a minimum curvature on the obstacles' boundaries.

Appendix G. Proof of Proposition 25

By Assumption 10, the shortest distance between the boundaries of obstacles i and j is greater than $2r$. If there exists an equilibrium point ($\dot{\boldsymbol{q}} = \boldsymbol{0}$) on the switching repulsion surface $\mathcal{S}_{ij}$, then by Eq. (10), we have that

$$\alpha(-\nabla\varphi_{\mathcal{R}_i}(\boldsymbol{q})) + (1-\alpha)(-\nabla\varphi_{\mathcal{R}_j}(\boldsymbol{q})) = \boldsymbol{0}. \tag{G.1}$$

Using the fact that $\delta_i = \delta_j$ on the switching surface, and writing the expressions for $-\nabla\varphi_{\mathcal{R}_i}$ and $-\nabla\varphi_{\mathcal{R}_j}$ using Eqs. (B.1) and (C.1), Eq. (G.1) becomes:

$$2g(\delta_s)\boldsymbol{e}_{\boldsymbol{q}} - \rho g'(\delta_s)\left(\alpha\boldsymbol{e}_{\boldsymbol{d}_i} + (1-\alpha)\boldsymbol{e}_{\boldsymbol{d}_j}\right) = \boldsymbol{0}, \tag{G.2}$$

where $\delta_s := \delta_i = \delta_j$. We now derive a conservative upper bound on the parameter k in the NLF $\varphi_{\mathcal{R}_i}$, defined by Eqs. (2) and (3). When the robot is on the switching repulsion surface, as illustrated in Fig. G.1, the repulsive force on it has the largest possible component in the direction opposite to $\boldsymbol{e}_{\boldsymbol{q}}$ when $\boldsymbol{e}_{\boldsymbol{d}_i} = \boldsymbol{e}_{\boldsymbol{d}_j}$[3] and $\boldsymbol{e}_{\boldsymbol{d}_i} = \boldsymbol{e}_{\boldsymbol{q}}$. By substituting $\boldsymbol{e}_{\boldsymbol{d}_i} = \boldsymbol{e}_{\boldsymbol{d}_j} = \boldsymbol{e}_{\boldsymbol{q}}$ into Eq. (G.2), we can reduce it to the scalar equation:

$$2g(\delta_s) - \rho g'(\delta_s) = 0. \tag{G.3}$$

To prevent the existence of an equilibrium point, and to ensure that the robot converges to the origin (the target position), the attraction term in this equation must exceed the repulsion term, i.e., $2g(\delta_s) > \rho g'(\delta_s)$. Using Eq. (3), this inequality can be simplified to $2\delta_s > k\rho$. From Assumption 10, the robot's radius r is the smallest possible value of δ_s, and from Assumption 11, the distance $2r_{\mathcal{D}} - 2r$ is the largest possible value of ρ (i.e., the longest straight-line distance that the robot's center can travel across the domain). Given this minimum value of δ_s and maximum value of ρ, the inequality $2\delta_s > k\rho$ becomes $2r > 2k(r_{\mathcal{D}} - r)$, which yields the following conservative upper bound on k:

$$k < r/(r_{\mathcal{D}} - r). \tag{G.4}$$

[3] This is a theoretical scenario that would not happen in practice; we use it here to find a conservative bound on k.

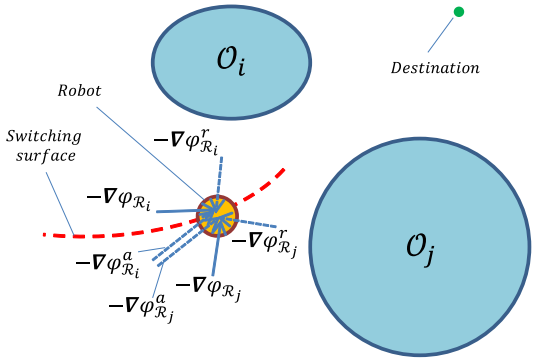

Fig. G.1. Illustration of the vector field components that act on a robot when it is located on a switching repulsion surface between two obstacles i and j. The vector field $\nabla\varphi_{\mathcal{R}_i}$, which defines the robot's controller on the side of the switching surface containing obstacle i, is the sum of an attractive component $\nabla\varphi^a_{\mathcal{R}_i}$ and a repulsive component $\nabla\varphi^r_{\mathcal{R}_i}$; the vector field $\nabla\varphi_{\mathcal{R}_j}$ is defined similarly. The theoretical scenario that results in Eq. (G.3) happens if $\nabla\varphi^a_{\mathcal{R}_i} + \nabla\varphi^a_{\mathcal{R}_j} = \nabla\varphi^r_{\mathcal{R}_i} + \nabla\varphi^r_{\mathcal{R}_j}$.

Appendix H. Proof of Corollary 26

The convex combination of vector fields $-\nabla\varphi_{\mathcal{R}_{\sigma_i}}$, $i \in \{1, \ldots, l\}$, is given by $\boldsymbol{\Upsilon}(\boldsymbol{q}) := \sum_{i=1}^{l} -\alpha_i\nabla\varphi_{\mathcal{R}_{\sigma_i}}(\boldsymbol{q})$, where $\alpha_i \in [0, 1]$ for all $i \in \{1, \ldots, l\}$ and $\sum_{i=1}^{l}\alpha_i = 1$. The differential inclusion in Eq. (9) and the expression in Eq. (10) for the robot dynamics in $\mathcal{S}_{\sigma_1\ldots\sigma_l}$ are redefined in terms of this convex combination $\boldsymbol{\Upsilon}(\boldsymbol{q})$. Then, if there exists an equilibrium point on $\mathcal{S}_{\sigma_1\ldots\sigma_l}$, by Eq. (10) we have that $\sum_{i=1}^{l}\alpha_i\nabla\varphi_{\mathcal{R}_{\sigma_i}}(\boldsymbol{q}) = \boldsymbol{0}$. Using the fact that $\delta_{\sigma_1} = \delta_{\sigma_2} = \cdots = \delta_{\sigma_l}$ on $\mathcal{S}_{\sigma_1\ldots\sigma_l}$, and writing $-\nabla\varphi_{\mathcal{R}_{\sigma_i}}$ in terms of Eqs. (B.1) and (C.1), this equation becomes:

$$2g(\delta_s)\boldsymbol{e}_{\boldsymbol{q}} - \rho g'(\delta_s)\left(\sum_{i=1}^{l}\alpha_i\boldsymbol{e}_{\boldsymbol{d}_{\sigma_i}}\right) = \boldsymbol{0}, \tag{H.1}$$

where $\delta_s := \delta_{\sigma_1} = \delta_{\sigma_2} = \cdots = \delta_{\sigma_l}$. Again, we consider the repulsive force on the robot with the largest possible component in the direction opposite to $\boldsymbol{e}_{\boldsymbol{q}}$, which occurs when $\boldsymbol{e}_{\boldsymbol{q}} = \boldsymbol{e}_{\boldsymbol{d}_{\sigma_1}} = \boldsymbol{e}_{\boldsymbol{d}_{\sigma_2}} = \cdots = \boldsymbol{e}_{\boldsymbol{d}_{\sigma_l}}$. This simplifies the sum in Eq. (H.1) to $\sum_{i=1}^{l}\alpha_i\,\boldsymbol{e}_{\boldsymbol{d}_{\sigma_i}} = \boldsymbol{e}_{\boldsymbol{q}}$, and the equation can be reduced to Eq. (G.3). This shows that choosing k small enough to satisfy Eq. (G.4) also guarantees the absence of an equilibrium on a switching repulsion surface that is equidistant from three or more obstacles.

Appendix I. Proof of Proposition 27

We follow the same procedure as in the proof of Proposition 25. An equilibrium point ($\dot{\boldsymbol{q}} = \boldsymbol{0}$) exists on the switching surface between $\mathcal{R}_i$ and $\mathcal{SS}$ if

$$\alpha(-\nabla\varphi_{\mathcal{SS}}(\boldsymbol{q})) + (1-\alpha)(-\nabla\varphi_{\mathcal{R}_i}(\boldsymbol{q})) = \boldsymbol{0}. \tag{I.1}$$

Using the fact that $\delta_i = \delta_c$ and, consequently, $g(\delta_i) = 1$ and $g'(\delta_i) = k/\delta_c$ on the boundary $\partial\mathcal{R}_i$ of $\mathcal{R}_i$, and writing the expressions for $-\nabla\varphi_{\mathcal{SS}}$ and $-\nabla\varphi_{\mathcal{R}_i}$ using Eqs. (A.1), (B.1), and (C.1), Eq. (I.1) becomes:

$$2\boldsymbol{e}_{\boldsymbol{q}} - (1-\alpha)(k/\delta_c)\rho\boldsymbol{e}_{\boldsymbol{d}_i} = \boldsymbol{0}. \tag{I.2}$$

On the switching surface, the repulsive force on the robot has the largest possible component in the direction opposite to $\boldsymbol{e_q}$ when $\boldsymbol{e_{d_i}} = \boldsymbol{e_q}$. In this case, we can reduce Eq. (I.2) to the scalar equation

$$2 - (1-\alpha)(k/\delta_c)\rho = 0. \tag{I.3}$$

To prevent the existence of an equilibrium point and ensure the robot's convergence to the origin, the attraction term in this equation must exceed the repulsion term:

$$2 > (1-\alpha)(k/\delta_c)\rho. \tag{I.4}$$

The right-hand side of Eq. (I.4) is maximized when $\alpha = 0$ and $\rho = 2r_{\mathcal{D}} - 2r$, the largest possible value of ρ. For these values of α and ρ, Eq. (I.4) can be rearranged as the following conservative upper bound on k:

$$k < \delta_c/(r_{\mathcal{D}} - r). \tag{I.5}$$

Appendix J. Proof of Corollary 28

We follow the same procedure as in the proof of Corollary 26. The convex combination of vector fields $-\nabla\varphi_{\mathcal{SS}}(\boldsymbol{q})$ and $-\nabla\varphi_{\mathcal{R}_{\sigma_i}}(\boldsymbol{q}), i \in \{1,\dots,l\}$, is given by $\boldsymbol{\Upsilon}(\boldsymbol{q}) := -\alpha_{ss}\nabla\varphi_{\mathcal{SS}}(\boldsymbol{q}) - \sum_{i=1}^{l}\alpha_i\nabla\varphi_{\mathcal{R}_{\sigma_i}}(\boldsymbol{q})$, where $\alpha_{ss},\ \alpha_i \in [0,1]$ for all $i \in \{1,\dots,l\}$ and $\alpha_{ss} + \sum_{i=1}^{l}\alpha_i = 1$. The differential inclusion in Eq. (9) and the expression in Eq. (10) for the robot dynamics on the switching surface are redefined in terms of $\boldsymbol{\Upsilon}(\boldsymbol{q})$. Thus, there is an equilibrium $\boldsymbol{q}$ on the switching surface if $\alpha_{ss}\nabla\varphi_{\mathcal{SS}}(\boldsymbol{q}) + \sum_{i=1}^{l}\alpha_i\varphi_{\mathcal{R}_{\sigma_i}}(\boldsymbol{q}) = \boldsymbol{0}$. Using the fact that $\delta_{\sigma_1} = \delta_{\sigma_2} = \cdots = \delta_{\sigma_l}$ on the switching surface, and writing $-\nabla\varphi_{\mathcal{SS}}$ and $-\nabla\varphi_{\mathcal{R}_{\sigma_i}}$ in terms of Eqs. (A.1), (B.1), and (C.1), this equation becomes:

$$2\left(\alpha_{ss} + g(\delta_s)\sum_{i=1}^{l}\alpha_i\right)\boldsymbol{e_q} - \rho g'(\delta_s)\left(\sum_{i=1}^{l}\alpha_i\boldsymbol{e_{d_{\sigma_i}}}\right) = \boldsymbol{0}, \tag{J.1}$$

where $\delta_s := \delta_{\sigma_1} = \delta_{\sigma_2} = \cdots = \delta_{\sigma_l}$. This distance equals δ_c on the boundaries of the repulsion spaces, and therefore on the switching surface, which implies that $g(\delta_s) = 1$ and $g'(\delta_s) = k/\delta_c$ on the switching surface. Using the fact that $\alpha_{ss} + \sum_{i=1}^{l}\alpha_i = 1$, Eq. (J.1) is reduced to

$$2\boldsymbol{e_q} - \rho(k/\delta_c)\left(\sum_{i=1}^{l}\alpha_i\boldsymbol{e_{d_{\sigma_i}}}\right) = \boldsymbol{0}. \tag{J.2}$$

On the switching surface, the largest possible repulsive force on the robot in the direction opposite to $\boldsymbol{e_q}$ occurs when $\boldsymbol{e_q} = \boldsymbol{e_{d_{\sigma_1}}} = \boldsymbol{e_{d_{\sigma_2}}} = \cdots = \boldsymbol{e_{d_{\sigma_l}}}$. Then, the sum in Eq. (J.2) is simplified to $\sum_{i=1}^{l}\alpha_i\,\boldsymbol{e_{d_{\sigma_i}}} = (\sum_{i=1}^{l}\alpha_i)\,\boldsymbol{e_q} = (1-\alpha_{ss})\boldsymbol{e_q}$, and the equation can be reduced to Eq. (I.3), with α_{ss} in place of α. Finally, setting the attraction term in the equation higher than the repulsion term to prevent the existence of an equilibrium point and to ensure the robot's convergence to the origin, we obtain the inequality in Eq. (I.4), with α_{ss} in place of α. This gives the same conservative upper bound on k as Eq. (I.5).

Appendix K. Proof of Lemma 30

The safe space NLF $\varphi_{\mathcal{SS}}(\boldsymbol{q})$ in Eq. (1) and the repulsion space NLF $\varphi_{\mathcal{R}_i}(\boldsymbol{q})$ in Eq. (2) are continuous functions by construction. We first consider the case where the robot crosses a switching repulsion surface $\mathcal{S}_{\sigma_1\dots\sigma_l}$ that lies within the intersection of $l \geq 2$ repulsion spaces $\mathcal{R}_{\sigma_1},\dots,\mathcal{R}_{\sigma_l}$, $\{\sigma_1,\dots,\sigma_l\} \subseteq \{0,1,\dots,m\}$. When the robot is on the switching surface, the distances δ_i, and hence the values of $g(\delta_i)$ and $\varphi_{\mathcal{R}_i}(\boldsymbol{q})$, are the same for all $i \in \{\sigma_1,\dots,\sigma_l\}$. Therefore, the NLFs $\varphi_{\mathcal{R}_i}(\boldsymbol{q})$, $i \in \{\sigma_1,\dots,\sigma_l\}$, are continuous at all points on this switching surface. In addition, we consider the case where the robot crosses a switching surface that lies within the intersection of the boundaries of $l \geq 1$ repulsion spaces $\mathcal{R}_{\sigma_1},\dots,\mathcal{R}_{\sigma_l}$, $\{\sigma_1,\dots,\sigma_l\} \subseteq \{0,1,\dots,m\}$, and is adjacent to $\mathcal{SS}$. When the robot is on the switching surface, the distances δ_i, $i \in \{\sigma_1,\dots,\sigma_l\}$, are all equal to δ_c, and therefore $g(\delta_i) = 1$, which implies that $\varphi_{\mathcal{R}_i}(\boldsymbol{q}) = \varphi_{\mathcal{SS}}(\boldsymbol{q})$. Thus, the NLFs $\varphi_{\mathcal{R}_i}(\boldsymbol{q})$, $i \in \{\sigma_1,\dots,\sigma_l\}$, and $\varphi_{\mathcal{SS}}(\boldsymbol{q})$ are continuous at all points on this switching surface.

Appendix L. Proof of Lemma 31

The time derivative of V_σ over $t \in [t_{\sigma,1}, t_{\sigma,2})$ is $\dot{V}_\sigma(t) = \dot{\varphi}_\sigma(t) = (\nabla\varphi_\sigma(\boldsymbol{q}(t)))^T\dot{\boldsymbol{q}}(t)$. Inserting the expression for $\dot{\boldsymbol{q}}$ from Eq. (7), we obtain $\dot{V}_\sigma(t) = -\|\nabla\varphi_\sigma(\boldsymbol{q}(t))\|^2$, which is non-positive in σ. Since V_σ is positive definite, which is straightforward to confirm, this expression for $\dot{V}_\sigma(t)$ indicates that V_σ is strictly decreasing over $t \in [t_{\sigma,1}, t_{\sigma,2})$. By LaSalle's invariance principle, the robot's trajectory converges to the largest invariant set in $\mathcal{E} = \{\boldsymbol{q} \in \sigma \mid \|\nabla\varphi_\sigma(\boldsymbol{q})\| = 0\}$, the set of critical points of φ_σ: the origin and non-zero norm critical points.

Appendix M. Proof of Theorem 32

Suppose a trajectory $\boldsymbol{q}(t)$ starts in $\mathcal{F}$ and outside $\mathcal{L}$, and then passes through a sequence of spaces $\sigma_1, \sigma_2, \dots, \sigma_n$, where each $\sigma_i \in \{\mathcal{SS}, \mathcal{R}_0, \mathcal{R}_1, \dots, \mathcal{R}_m\}$. Then the corresponding functions $V_{\sigma_1}(\boldsymbol{q}), V_{\sigma_2}(\boldsymbol{q}), \dots, V_{\sigma_n}(\boldsymbol{q})$ comprise a sequence of strictly decreasing functions (Lemma 31), for which $V_{\sigma_i}(\boldsymbol{q}(t)) = V_{\sigma_{i+1}}(\boldsymbol{q}(t))$ at the time $t = t_{\sigma_{i+1},1}$ when the trajectory leaves σ_i and enters σ_{i+1} (Lemma 30). Given that k satisfies the bound in Theorem 29, we can invoke Theorem 3.1 in Liberzon (2003) to conclude that the existence of this continuous sequence of strictly decreasing, positive definite functions indicates that $\boldsymbol{q}(t)$ converges asymptotically to a critical point of φ_{σ_n}. Since $\boldsymbol{q}(t)$ starts outside $\mathcal{L}$, this point cannot be a non-zero norm critical point, and the origin is the only remaining candidate. Thus, $\boldsymbol{q}(t)$ asymptotically converges to the origin. On the other hand, if a trajectory starts on the stable manifold $l \in \mathcal{L}$ of a non-zero norm critical point $\boldsymbol{q}^*$, then it asymptotically converges to $\boldsymbol{q}^*$. Since $\mathcal{L}$ is a set of measure zero in $\mathcal{F}$, we cannot establish basins of attraction of the non-zero norm critical points. This implies that the origin is an almost globally asymptotically stable equilibrium point of system (6).

Appendix N. Proof of Corollary 33

We know that $\varphi_\sigma(\boldsymbol{q}) \in [0,1)$ for each space $\sigma \in \{\mathcal{SS}, \mathcal{R}_0, \mathcal{R}_1, \dots, \mathcal{R}_m\}$, and therefore $\varphi_\sigma(\boldsymbol{q}(0)) \in [0,1)$ for $\boldsymbol{q}(0) \in \mathcal{F}$. If $\boldsymbol{q}(0) \notin \mathcal{L}$, then from the proof of Theorem 32, there is a sequence of strictly decreasing, positive definite functions $V_{\sigma_1}(\boldsymbol{q})$, $V_{\sigma_2}(\boldsymbol{q})$, ..., $V_{\sigma_n}(\boldsymbol{q})$ which correspond to the sequence of spaces $\sigma_1, \sigma_2, \dots, \sigma_n$ that the trajectory $\boldsymbol{q}(t)$ passes through. This implies that for each $\sigma \in \{\sigma_1, \sigma_2, \dots, \sigma_n\}$, $\varphi_\sigma(\boldsymbol{q}(t)) \in [0,1)$ for all $t \geq 0$. Thus, the robot's trajectory remains in $\mathcal{F}$ for all $t \geq 0$, and so the robot never collides with the domain boundary, where $\varphi_{\mathcal{R}_0} = 1$, or the boundary of an obstacle i, where $\varphi_{\mathcal{R}_i} = 1$. If $\boldsymbol{q}(0) \in l$, where $l \in \mathcal{L}$ is the stable manifold of a non-zero norm critical point $\boldsymbol{q}^*$, then the trajectory $\boldsymbol{q}(t)$ monotonically converges to $\boldsymbol{q}^*$ due to the robot's first-order dynamics. Therefore, the trajectory also remains in $\mathcal{F}$, and so the robot does not collide with the boundary of an obstacle or the domain boundary.

References

Ames, A. D., Xu, X., Grizzle, J. W., & Tabuada, P. (2017). Control barrier function based quadratic programs for safety critical systems. *IEEE Transactions on Automatic Control*, *62*(8), 3861–3876.

Angélico, B. A., Chamon, L. F., Paternain, S., Ribeiro, A., & Pappas, G. J. (2021). Source seeking in unknown environments with convex obstacles. In *Proc. am. control conf.* (pp. 5055–5061).

Arslan, O., & Koditschek, D. E. (2019). Sensor-based reactive navigation in unknown convex sphere worlds. *The International Journal of Robotics Research*, *38*(2–3), 196–223.

Arslan, O., Pacelli, V., & Koditschek, D. E. (2017). Sensory steering for sampling-based motion planning. In *IEEE/RSJ int. conf. intell. robots syst.* (pp. 3708–3715).

Autonomous Collective Systems Lab YouTube channel (2021). Local navigation-like functions for safe robot navigation in bounded domains with unknown convex obstacles. https://www.youtube.com/watch?v=OoCYusrAuTY.

Bertsekas, D. P., Nedich, A., & Ozdaglar, A. E. (2003). *Convex analysis and optimization*. Athena Scientific.

Chen, Y., Singletary, A., & Ames, A. D. (2021). Guaranteed obstacle avoidance for multi-robot operations with limited actuation: A control barrier function approach. *IEEE Control Systems Letters*, *5*(1), 127–132.

Conner, D. C., Rizzi, A. A., & Choset, H. (2003). Composition of local potential functions for global robot control and navigation. In *IEEE/RSJ int. conf. intell. robots syst.* (pp. 3546–3551).

Constantinou, N., & Loizou, S. G. (2020). Robot navigation on star worlds using a single-step navigation transformation. In *Proc. IEEE conf. decis. control* (pp. 1537–1542).

Farivarnejad, H., & Berman, S. (2020). Design and analysis of a potential-based controller for safe robot navigation in unknown GPS-denied environments with strictly convex obstacles. *Systems & Control Letters*, *144*, Article 104772.

Filippidis, I., & Kyriakopoulos, K. J. (2011). Adjustable navigation functions for unknown sphere worlds. In *Proc. IEEE conf. decis. control & eur. control conf.* (pp. 4276–4281).

Fox, D., Burgard, W., & Thrun, S. (1997). The dynamic window approach to collision avoidance. *IEEE Robotics & Automation Magazine*, *4*(1), 23–33.

Ge, S. S., & Cui, Y. J. (2000). New potential functions for mobile robot path planning. *IEEE Transactions on Robotics and Automation*, *16*(5), 615–620.

Ge, S. S., & Cui, Y. J. (2002). Dynamic motion planning for mobile robots using potential field method. *Autonomous Robots*, *13*(3), 207–222.

Guldner, J., & Utkin, V. I. (1995). Sliding mode control for gradient tracking and robot navigation using artificial potential fields. *IEEE Transactions on Robotics and Automation*, *11*(2), 247–254.

Ibuki, T., Wilson, S., Ames, A. D., & Egerstedt, M. (2020). Distributed collision-free motion coordination on a sphere: A conic control barrier function approach. *IEEE Control Systems Letters*, *4*(4), 976–981.

Khalil, H. K. (1996). *Nonlinear systems*. Upper Saddle River, N.J.: Prentice Hall.

Khatib, O. (1986). Real-time obstacle avoidance for manipulators and mobile robots. *The International Journal of Robotics Research*, *5*(1), 90–98.

Kim, J.-O., & Khosla, P. K. (1992). Real-time obstacle avoidance using harmonic potential functions. *IEEE Transactions on Robotics and Automation*, *8*(3), 338–349.

Koditschek, D. E., & Rimon, E. (1990). Robot navigation functions on manifolds with boundary. *Advances in Applied Mathematics*, *11*(4), 412–442.

Kumar, H., Paternain, S., & Ribeiro, A. (2019). Navigation of a quadratic potential with ellipsoidal obstacles. In *Proc. IEEE conf. decis. control* (pp. 4777–4784).

Kumar, H., Paternain, S., & Ribeiro, A. (2020). Navigation of a quadratic potential with star obstacles. In *Proc. am. control conf.* (pp. 2043–2048).

Lafmejani, A. S., Farivarnejad, H., & Berman, S. (2021). Adaptation of gradient-based navigation control for holonomic robots to nonholonomic robots. *IEEE Robotics and Automation Letters*, *6*(1), 191–198.

Li, C., & Tanner, H. G. (2019). Navigation functions with time-varying destination manifolds in star worlds. *IEEE Transactions on Robotics*, *35*(1), 35–48.

Liberzon, D. (2003). *Switching in systems and control*. Springer Science & Business Media.

Loizou, S. G. (2017). The navigation transformation. *IEEE Transactions on Robotics*, *33*(6), 1516–1523.

Ogren, P., & Leonard, N. E. (2005). A convergent dynamic window approach to obstacle avoidance. *IEEE Transactions on Robotics*, *21*(2), 188–195.

Paternain, S., Koditschek, D. E., & Ribeiro, A. (2018). Navigation functions for convex potentials in a space with convex obstacles. *IEEE Transactions on Automatic Control*, *63*(9), 2944–2959.

Paternain, S., Mokhtari, A., & Ribeiro, A. (2018). A Newton method for faster navigation in cluttered environments. In *Proc. IEEE conf. decis. control* (pp. 4084–4090).

Paternain, S., & Ribeiro, A. (2017). Safe online navigation of convex potentials in spaces with convex obstacles. In *Proc. IEEE conf. decis. control* (pp. 2473–2478).

Pierson, A., Vasile, C., Gandhi, A., Schwarting, W., Karaman, S., & Rus, D. (2019). Dynamic risk density for autonomous navigation in cluttered environments without object detection. In *IEEE int. conf. robot. autom.* (pp. 5807–5814).

Prajna, S., Jadbabaie, A., & Pappas, G. J. (2004). Stochastic safety verification using barrier certificates. In *Proc. IEEE conf. decis. control* (pp. 929–934).

Ramírez-Llanos, E., & Martínez, S. (2019). Stochastic source seeking for mobile robots in obstacle environments via the SPSA method. *IEEE Transactions on Automatic Control*, *64*(4), 1732–1739.

Rimon, E., & Koditschek, D. E. (1992). Exact robot navigation using artificial potential functions. *IEEE Transactions on Robotics and Automation*, *8*(5), 501–518.

Robotis (2021). TurtleBot3 Burger. https://www.robotis.us/turtlebot-3-burger-us/.

Shahidi, R., Shayman, M., & Krishnaprasad, P. S. (1991). Mobile robot navigation using potential functions. In *IEEE int. conf. robot. autom.* (pp. 2047–2053).

Tanner, H. G., Jadbabaie, A., & Pappas, G. J. (2003). Stable flocking of mobile agents, part I: fixed topology. In *Proc. IEEE conf. decis. control, Vol. 2* (pp. 2010–2015).

Vasilopoulos, V., Pavlakos, G., Bowman, S. L., Caporale, J. D., Daniilidis, K., Pappas, G. J., et al. (2020). Reactive semantic planning in unexplored semantic environments using deep perceptual feedback. *IEEE Robotics and Automation Letters*, *5*(3), 4455–4462.

Vasilopoulos, V., Vega-Brown, W., Arslan, O., Roy, N., & Koditschek, D. E. (2018). Sensor-based reactive symbolic planning in partially known environments. In *IEEE int. conf. robot. autom.* (pp. 5683–5690).

Wang, L., Ames, A. D., & Egerstedt, M. (2017). Safety barrier certificates for collisions-free multirobot systems. *IEEE Transactions on Robotics*, *33*(3), 661–674.

Hamed Farivarnejad received the Master's degree and the Ph.D. degree in Mechanical Engineering from K.N. Toosi University of Technology and Arizona State University (ASU), respectively in 2009 and 2020. He served as a Postdoctoral Research Scholar in ASU in 2021. He then changed direction to industry, where he served as a Robotics Engineer and a GNC Engineer at Redwire Space and E-Space in 2022 and 2023. He currently works as a Staff Controls Engineer at GE Aerospace. His research interests lie within the fields of nonlinear control theory, robotics, and multi-robot systems.

Amir Salimi Lafmejani received the Master's degree in Mechatronics Engineering with a focus in robotics from the University of Tehran in 2017 and the Ph.D. degree in Electrical Engineering with a specialization in control systems from Arizona State University in 2022. He is currently a Senior Robotics Software Engineer in the robotics industry. His research endeavors focus primarily on the control of mobile robots.

Spring Berman received the M.S.E. and Ph.D. degrees in Mechanical Engineering and Applied Mechanics from the University of Pennsylvania in 2008 and 2010, respectively. From 2010 to 2012, she was a Postdoctoral Fellow in Computer Science at Harvard University. She was then an Assistant Professor of Mechanical and Aerospace Engineering at Arizona State University, where she has been an Associate Professor since 2018. Her research focuses on the synthesis of control strategies, including bio-inspired controllers, for robotic swarms and other types of distributed systems.